Journal of Magnetic Resonance **153,** 155–177 (2001)
doi:10.1006/jmre.2001.2340, available online at http://www.idealibrary.com on IDEAL®

ADVANCES IN MAGNETIC RESONANCE

The Return of the Frequency Sweep: Designing Adiabatic Pulses for Contemporary NMR

Michael Garwood and Lance DelaBarre

Center for Magnetic Resonance Research and Department of Radiology, University of Minnesota, Minneapolis, Minnesota 55455

Received October 18, 2000; revised February 22, 2001

Frequency-modulated (FM) pulses that function according to adiabatic principles are becoming increasingly popular in many areas of NMR. Often adiabatic pulses can extend experimental capabilities and minimize annoying experimental imperfections. Here, adiabatic principles and some of the current methods used to create these pulses are considered. The classical adiabatic rapid passage, which is a fundamental element upon which all adiabatic pulses and sequences are based, is analyzed using vector models in different rotating frames of reference. Two methods to optimize adiabaticity are described, and ways to tailor modulation functions to best satisfy specific experimental needs are demonstrated. Finally, adiabatic plane rotation pulses and frequency-selective multiple spin-echo sequences are considered. © 2001 Elsevier Science

I. INTRODUCTION

The emergence of pulsed NMR in the 1960s (*1*) stimulated much interest in the design of RF pulses, which is now an important area of research in NMR. During the past few decades, work on RF pulses has resulted in many new ways to manipulate nuclear spins and has produced valuable methods to overcome annoying experimental imperfections. In recent years, this area of research has experienced a surge of activity due in part to the widespread availability of NMR instruments with hardware and software supporting the use of shaped RF pulses. The ability to continuously modulate pulse amplitude and phase (or frequency) is a standard feature of most modern NMR spectrometers, whereas just over a decade ago, many commercial systems did not permit amplitude modulation and could perform only low resolution phase shifts (e.g., in steps of multiples of 90°). The ability to modulate both pulse amplitude and phase continuously has brought about renewed interest in an approach used in the early days of NMR (*2, 3*). In those early experiments, NMR signals were excited by sweeping the effective magnetic field $\mathbf{B}_{\mathbf{eff}}$ slowly (adiabatically) so that the bulk magnetization vector $\mathbf{M}$ remained approximately collinear with $\mathbf{B}_{\mathbf{eff}}$. One experimental advantage of this type of adiabatic sweep (or passage) is the ability to accomplish excitation over a broad band of resonant frequencies with a high degree of tolerance to RF field inhomogeneity. In early NMR experiments, adiabatic passage was performed by sweeping the amplitude of the polarizing magnetic field B_0 in the presence of continuous wave RF irradiation. Nowadays, an adiabatic passage is more often performed by sweeping the pulse frequency $\omega_{\mathrm{RF}}(t)$, while B_0 remains constant.

To provide utility in contemporary NMR applications, adiabatic rotations must be accomplished rapidly relative to the relaxation times, T_1 and T_2. Thus, the process is often termed adiabatic *rapid* passage (*4*). Significant research effort has focused on the design of modulation functions which improve the efficiency of adiabatic rapid passage (*5–16*). In this work, different approaches to optimizing modulation functions will be discussed.

As an alternative to frequency-modulating the pulse, a more common and equivalent approach is to modulate the phase of the pulse according to the function

$$\phi(t) = \int_0^t (\omega_{\mathrm{RF}}(t') - \omega_{\mathrm{c}})\, dt' + \phi(0), \qquad [1]$$

where ω_{c} is the carrier frequency (the center frequency in the bandwidth of interest). To facilitate a classical understanding, in this work vector analyses will be based on frequency-modulated (FM) adiabatic pulses, even though in practice the phase-modulated version is most often used.

Adiabatic pulses are becoming increasingly popular in a number of different applications. *In vivo* NMR experiments are often performed with a surface transceiver coil that maximizes sensitivity, but has the disadvantage of producing a highly inhomogeneous RF field (B_1). When a surface coil is used to transmit conventional pulses, spatial variations in flip angle lead to sensitivity losses, quantification errors, and undesirable coherences. As a consequence, *in vivo* NMR experiments are often performed with adiabatic pulses which have the capability to generate uniform rotations of $\mathbf{M}$ even when B_1 is highly inhomogeneous. Although commercial RF coils used for high-resolution NMR are generally considered to provide highly uniform B_1 profiles, sensitivity gains have also been observed when conventional

1090-7807/01 $35.00

"square" pulses were replaced by adiabatic pulses in certain high resolution NMR sequences (*17–20*).

In many areas of NMR, the pursuit of increased sensitivity and spectral resolution continues to propel further increases in magnetic field. Ultra-high field NMR can benefit from the ability of certain adiabatic pulses to cover broad bandwidths while minimizing RF power dissipation. As an example, previous work has shown that adiabatic pulses can significantly reduce RF power requirements in spin decoupling (*21–27*). This approach is advantageous for the multitude of popular NMR experiments in which insensitive nuclei (e.g., ^{13}C and ^{15}N) are detected indirectly via scalar coupling with ^{1}H. *In vivo* NMR experiments sometimes encounter the problem of insufficient peak B_1, but this limitation can be circumvented by using certain types of adiabatic pulses that operate over broad bandwidths with low peak RF power. When *in vivo* NMR is performed with spatially-selective RF pulses, a frequency shift, such as chemical shift, has the effect of displacing the volume of interest. This problem can be minimized by using adiabatic pulses that excite broad bandwidths in a highly selective manner. Finally, at the high frequencies used in ultra-high field NMR, conditions may become favorable for dielectric resonances which can have detrimental effects on B_1 homogeneity (*28*). Adiabatic pulses can provide a way to deal with this problem as well.

In the early years, the number of parameters that could be varied in the process of creating new RF pulses was limited by practical considerations, such as the inability of spectrometers to generate small phase shifts. Despite these restrictions, over two decades ago Levitt and Freeman introduced a novel approach to compensate for experimental non-idealities using a train of phase-modulated pulses, collectively known as a composite pulse (*29*). The general principle in the design of composite pulses is to make the individual pulses cancel each other's imperfections. Despite the fact that the phase shifts used in composite pulses are generally much courser than those used nowadays in adiabatic pulses, a variety of useful composite pulses have been developed to excite spin systems in particular ways and to compensate for experimental imperfections (for a sampling, see (*29–46*) and references therein). To date, composite pulses still offer the best approach to many types of NMR experiments.

Many adiabatic pulses are closely related to composite pulses. In the past, composite pulses have been derived from adiabatic principles (*5, 37*), and conversely, the performance of certain adiabatic pulses (*17, 47*) has been improved using expansion procedures that were originally developed for composite pulses (*38, 39*). As compared with composite pulses, adiabatic pulses derived from such expansion procedures generally offer the greatest combined immunity to RF inhomogeneity and resonance offset for a given amount of RF power. Such gains in performance result from the fact that the expanded adiabatic sequences are based on adiabatic rapid passage, which is already self-compensated for RF inhomogeneity.

The applicability of the adiabatic rapid passage is restricted to a small subset of pulsed NMR experiments, since the $\mathbf{B}_{\mathbf{eff}}(t)$ trajectory dictates the rotation only for the component of **M** that is collinear with $\mathbf{B}_{\mathbf{eff}}(t)$. When **M** is perpendicular to $\mathbf{B}_{\mathbf{eff}}$ during the adiabatic passage, a variable flip angle is produced, since different isochromats evolve at different rates about $\mathbf{B}_{\mathbf{eff}}$. Furthermore, for these perpendicular components of **M**, the net rotation axis is dependent on the initial orientation of **M**. Finally, immunity to RF inhomogeneity is attained only when the final $\mathbf{B}_{\mathbf{eff}}$ orientation is on the transverse plane or along the longitudinal axis. For these reasons, previous work in this area has generally focused on the two basic transformations that can be properly achieved with adiabatic rapid passage. These include: 1) rotating longitudinal magnetization M_z onto the transverse plane (excitation) and 2) population inversion ($M_z \rightarrow -M_z$). The specific types of $\mathbf{B}_{\mathbf{eff}}$ sweeps that accomplish these tasks are known as adiabatic half-passage (AHP) and full-passage (AFP), respectively.

Many NMR experiments require a pulse to perform transformations about a rotation axis that remains invariant for all isochromats, regardless of the initial orientation of **M**. For example, to generate optimal signal with a spin echo sequence (90°-τ-180°-τ-acquire), the rotation axis of the 180° pulse must remain insensitive to changes in resonance offset and B_1 amplitude. As mentioned above, a conventional AFP is not suitable for performing this type of transformation, which is sometimes called a *plane rotation*. Plane rotations can be performed with composite adiabatic pulses that were first developed just over a decade ago (*47–56*). With these composite adiabatic pulses, NMR experiments that previously required a uniform B_1 to rotate spins by the correct angles can now be performed with unprecedented insensitivity to B_1 inhomogeneity.

In this work, we consider some of the current principles and methods used to create adiabatic pulses. We begin with a classical explanation of the adiabatic rapid passage, which is a fundamental element upon which all adiabatic pulses and sequences are based (Section II). We then explore the adiabatic condition and how it can be used to generate modulation functions tailored to meet specific performance criteria (Section III). Finally, adiabatic plane rotation pulses are described (Section IV).

II. CLASSICAL TREATMENT OF ADIABATIC RAPID PASSAGE

IIA. The Hyperbolic Secant Pulse in Two Different Frames of Reference

Undoubtedly the most popular AFP is the hyperbolic secant (HS1) pulse (*5, 57, 58*), which originated from the self-induced transparency effect observed in coherent optical spectroscopy (*59*). Using a form similar to Silver *et al.* (*57*), the HS1 pulse can be written as

$$\omega_1(t) = \omega_1^{\max}(\mathrm{sech}(\beta t))^{1+i\mu}, \qquad [1]$$

where $\omega_1^{\max}$ is the maximum pulse amplitude in rad/s, and β and

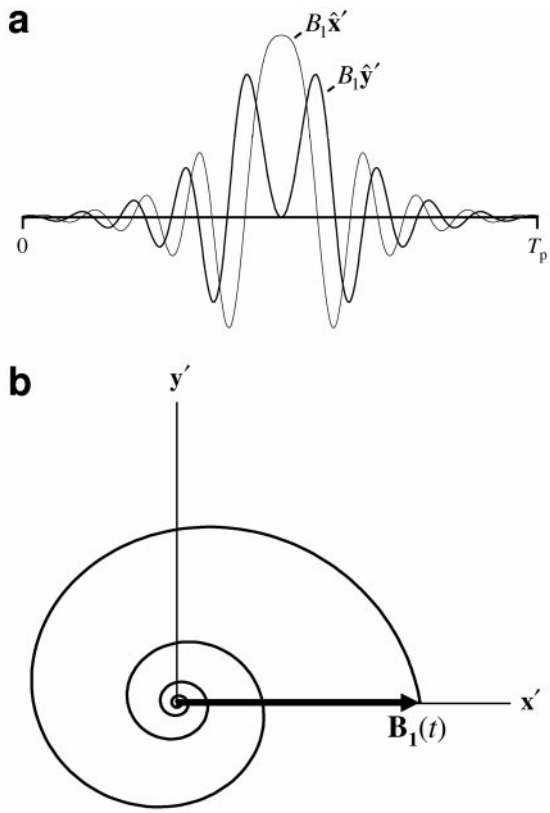

FIG. 1. The magnetic field components of the hyperbolic secant (HS1) pulse in a reference frame that rotates at a constant carrier frequency, called the phase-modulated (PM) frame. (a) Time dependence of the real ($B_1\hat{\mathbf{x}}'$) and imaginary ($B_1\hat{\mathbf{y}}'$) components as viewed from the PM frame. (b) Starting at the origin of PM frame, $\mathbf{B_1}(t)$ spirals out to a maximum value, and then spirals back.

μ are real constants. In an alternative form, Eq. [1] becomes

$$\omega_1(t) = \omega_1^{\max}\mathrm{sech}(\beta t)\, e^{i\phi(t)}, \qquad [2]$$

where

$$\phi(t) = \mu(\ln(\mathrm{sech}(\beta t))). \qquad [3]$$

This representation describes the HS1 pulse in a reference frame that rotates at a constant carrier frequency ω_c. This reference frame is appropriately called the phase-modulated (PM) frame because the pulse phase ϕ varies in time (5). Figure 1 shows plots of the HS1 pulse as viewed from the PM frame.

Adiabatic pulses can also be described in terms of a frequency modulation. Accordingly, the HS1 pulse is described by the amplitude modulated (AM) function

$$\omega_1(t) = \omega_1^{\max}\mathrm{sech}(\beta t) \qquad [4]$$

and the FM function

$$\omega_{\mathrm{RF}}(t) - \omega_c = \frac{d\phi}{dt} = -\mu\beta\tanh(\beta t)\,. \qquad [5]$$

This form of the pulse can be described in a frame of reference that rotates in concert with a variable pulse frequency $\omega_{\mathrm{RF}}(t)$. This frame is known as the frequency-modulated (FM) frame. In the FM frame, the orientation of $\boldsymbol{\omega_1}$ remains stationary during an adiabatic passage.

From Eqs. [4] and [5], it is apparent why the HS1 pulse is sometimes called the sech/tanh pulse. To permit a general nomenclature to facilitate comparisons of HS1 pulses with other adiabatic pulses, we choose to replace $\mu\beta$ by a single variable A (the amplitude of the frequency modulation), while β is treated as a dimensionless truncation factor (typically set so that $\mathrm{sech}(\beta) = 0.01$). As such, the HS1 pulse can be written as

$$\omega_1(t) = \omega_1^{\max}\mathrm{sech}(\beta(2t/T_p - 1)), \qquad [6]$$

$$\omega_{\mathrm{RF}}(t) - \omega_c = A\tanh(\beta(2t/T_p - 1)), \qquad [7]$$

where T_p is pulse length.

IIB. Visualizing Adiabatic Sweeps in the FM Frame

The motion of the magnetic field components of an adiabatic pulse and its effect on a magnetization vector are most easily visualized in a frequency-modulated frame. To differentiate between different FM frames, we will refer to them by one of their characteristic rotation frequencies. Hence, the FM frame described above will be called the "ω_{RF} frame." As illustrated in Fig. 2, in the ω_{RF} frame the effective magnetic field $\boldsymbol{\omega_{\mathrm{eff}}}(t)$ is the vector sum of the field components,

$$\boldsymbol{\omega_1} = \gamma B_1\hat{\mathbf{x}}' \qquad [8]$$

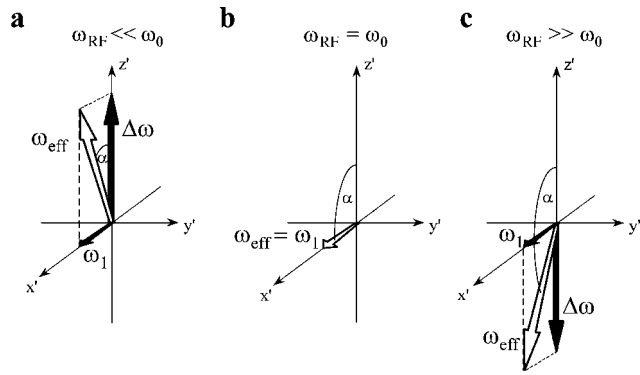

FIG. 2. The effective field vector $\boldsymbol{\omega_{\mathrm{eff}}}$ and its components, $\boldsymbol{\omega_1}$ and $\boldsymbol{\Delta\omega}$, in a frequency modulated (FM) frame of reference. The FM frame rotates with a variable angular frequency set by the frequency modulation ($\omega_{\mathrm{RF}}(t)$) used in the pulse. The FM frame is also referred to as the ω_{RF} frame. The three conditions shown correspond to (a) far below resonance, (b) at resonance, and (c) far above resonance.

$$\Delta\boldsymbol{\omega}(t) = (\omega_0 - \omega_{\mathrm{RF}}(t))\hat{\mathbf{z}}', \quad [9]$$

where ω_0 is the Larmor frequency of a given spin. During the adiabatic passage, $\boldsymbol{\omega}_{\mathbf{eff}}(t)$ changes its orientation at the instantaneous angular velocity, $d\alpha/dt$, where

$$\alpha(t) = \arctan\left[\frac{\omega_1(t)}{\Delta\omega(t)}\right]. \quad [10]$$

To facilitate an understanding of adiabatic passage, for the moment let $\boldsymbol{\omega}_{\mathbf{1}}$ have a constant amplitude along the x' axis of the ω_{RF} frame ($\phi = 0$). If the pulse frequency starts far below resonance ($\omega_{\mathrm{RF}} \ll \omega_0$), $\Delta\omega$ is initially very large relative to ω_1. Thus, $\omega_{\mathrm{eff}} \approx \Delta\omega$ and the initial orientation of $\boldsymbol{\omega}_{\mathbf{eff}}$ is approximately collinear with z' (Fig. 2a). As $\omega_{\mathrm{RF}}(t)$ begins to increase, $\Delta\omega(t)$ decreases and $\boldsymbol{\omega}_{\mathbf{eff}}$ rotates toward the transverse plane. With an AHP, $\omega_{\mathrm{RF}}(t)$ terminates at resonance ω_0, at which time $\boldsymbol{\omega}_{\mathbf{eff}} = \boldsymbol{\omega}_{\mathbf{1}}$ (Fig. 2b). To perform an AFP, the frequency sweep continues past resonance toward the negative extreme, leading to a final $\boldsymbol{\omega}_{\mathbf{eff}}$ orientation along $-z'$ (Fig. 2c). During the sweep, $\mathbf{M}$ follows $\boldsymbol{\omega}_{\mathbf{eff}}(t)$ provided that

$$|\omega_{\mathrm{eff}}(t)| \gg |d\alpha/dt|, \quad [11]$$

for all time (*4*). Also known as the "adiabatic condition," this inequality represents the main guiding principle that is used in the design and optimization of modulation functions for adiabatic rapid passage (Section III).

It is also instructive to consider how this process occurs for different isochromats. To facilitate this analysis, the pulse frequency is expressed as the sum of the carrier frequency plus a FM function,

$$\omega_{\mathrm{RF}}(t) = \omega_{\mathrm{c}} + AF_2(t), \quad [12]$$

where A is the amplitude of the frequency modulation (relative to the center frequency, ω_{c}) and $F_2(t)$ is a dimensionless driving function which varies between -1 to 1. Upon substitution of Eq. [12] into Eq. [9], the longitudinal component in ω_{RF} frame becomes

$$\Delta\boldsymbol{\omega}(t) = [\Omega - AF_2(t)]\hat{\mathbf{z}}', \quad [13]$$

where Ω ($=\omega_0 - \omega_{\mathrm{c}}$) is the resonance offset of a given isochromat. As illustrated in Fig. 3, the trajectory of $\boldsymbol{\omega}_{\mathbf{eff}}(t)$, as well as the time of resonance (t_Ω), depend on Ω. It can be seen that only a single isochromat can be rotated by exactly 90° with an AHP. The net rotation of other isochromats depends on the sign and magnitude of the resonance offset, as well as the amplitude of $\boldsymbol{\omega}_{\mathbf{1}}$. The only way to minimize such offset-dependent excitation with an AHP is to increase the amplitude of $\boldsymbol{\omega}_{\mathbf{1}}$ at the end of the pulse.

Conversely, with an AFP, the total angle subtended by $\boldsymbol{\omega}_{\mathbf{eff}}$ approaches 180° for all isochromats provided that

$$|\Omega| \ll A \quad [14]$$

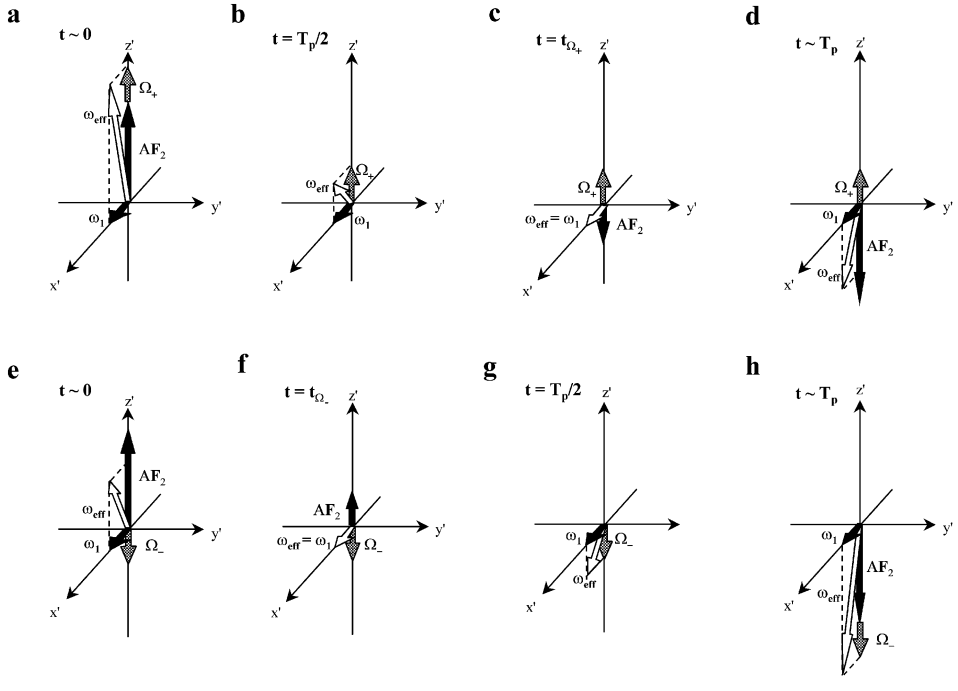

FIG. 3. The time dependence of the $\boldsymbol{\omega}_{\mathbf{eff}}$ trajectory during an adiabatic passage as seen by an isochromat with (a–d) positive and (e–h) negative frequency offsets in the ω_{RF} frame. Each isochromat (Ω_+ and Ω_-) reaches resonance at different times ($t_{\Omega+}$ and $t_{\Omega-}$).

and that $\Delta\omega$ is much greater than ω_1 at the beginning ($t = 0$) and end ($t = T_p$) of the sweep. If the latter condition is not satisfied, $\boldsymbol{\omega_{eff}}$ no longer approaches the longitudinal axis at one or both of these times, and consequently, the resultant sweep angle is $<180^\circ$. This normally occurs for isochromats just inside the boundaries of the frequency sweep, where $|\Omega|$ is only slightly less than A. One way to achieve a more uniform inversion over the complete range of the frequency sweep ($\pm A$) is to employ an AM function $\omega_1(t)$ that smoothly approaches zero at its beginning and end. The advantage of this approach can be revealed by observing the time dependence of the longitudinal magnetization ($M_z(t)$) in response to AFPs with different $\omega_1(t)$ functions. The AFPs chosen for the present comparison were: 1) chirp, which employs a constant ω_1 (60), and 2) the HS1 pulse which uses the hyperbolic secant function for $\omega_1(t)$. Figure 4 shows the AM and FM shapes for these pulses, along with $M_z(t)$ obtained by numerically solving the Bloch equations. For each case, $M_z(t)$ is shown for three different isochromats which achieve resonance at different times (t_Ω) determined by the condition, $AF_2(t) = \Omega$. Because ω_1 is constant in chirp (Fig. 4a–c), oscillations in $M_z(t)$ arise from the lack of alignment between $\boldsymbol{\omega_{eff}}$ and $\mathbf{M}$, which worsen for Ω values approaching the initial frequency, $AF_2(0)$. Similarly, for isochromats that reach resonance late in the frequency sweep, the final orientation of $\boldsymbol{\omega_{eff}}$ does not align with $-z'$. These phenomena equivalently reduce the degree of inversion attained by isochromats near both extremes of the frequency sweep. Conversely, with an HS1 pulse (Fig. 4d–f), more uniform inversion can occur because $\omega_1(t)$ allows $\boldsymbol{\omega_{eff}}$ to be approximately collinear with z' at the beginning and end of the sweep for all isochromats.

IIC. A Doubly Rotating Frame of Reference: The ω_{eff} Frame

Vector descriptions in the ω_{RF} frame are useful for elucidating how AHP and AFP pulses are able to induce near perfect 90° and 180° flip angles despite spatial variations in the RF

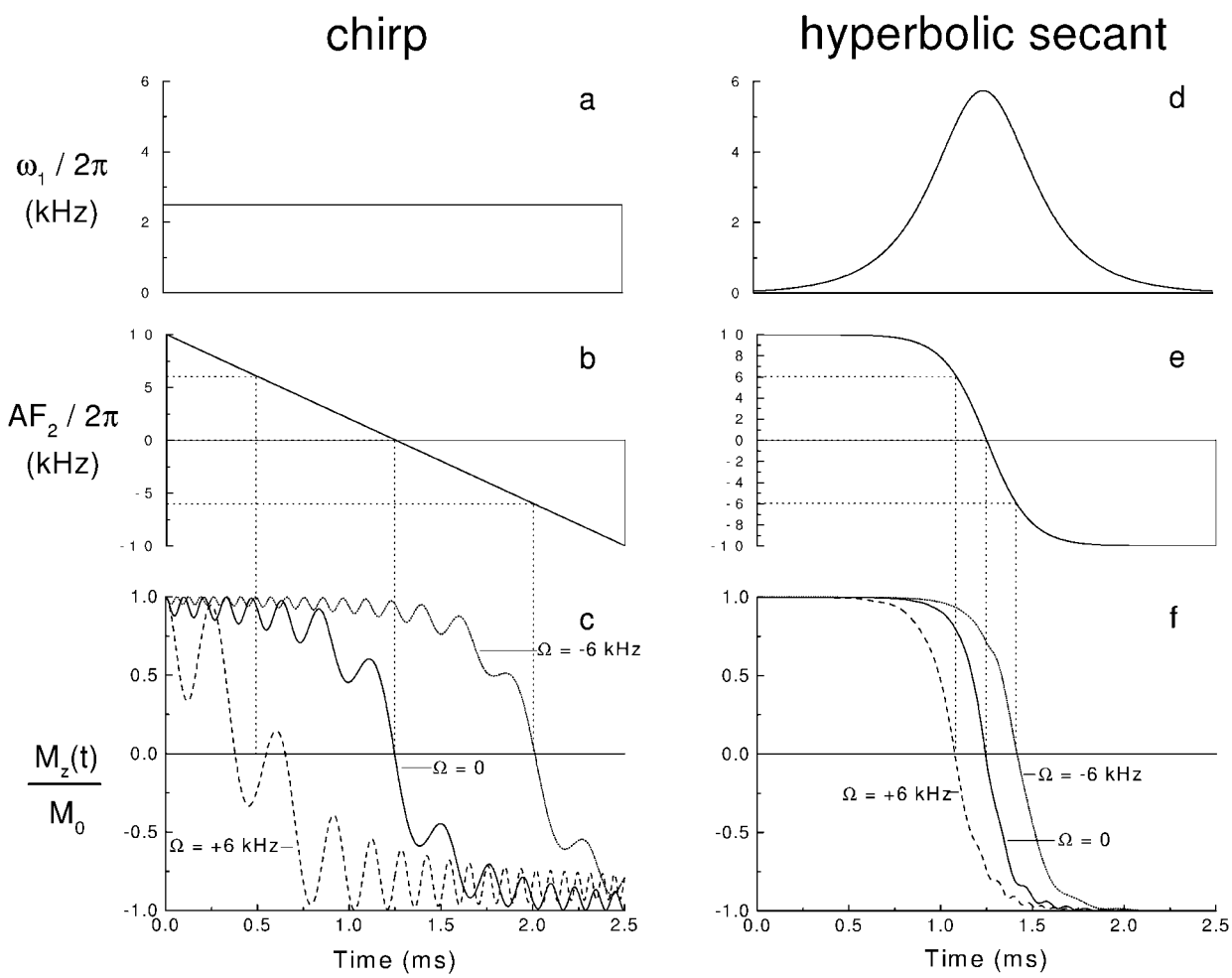

FIG. 4. AM and FM functions of the chirp and hyperbolic secant (HS1) pulses, and their effects on longitudinal magnetization (M_z).

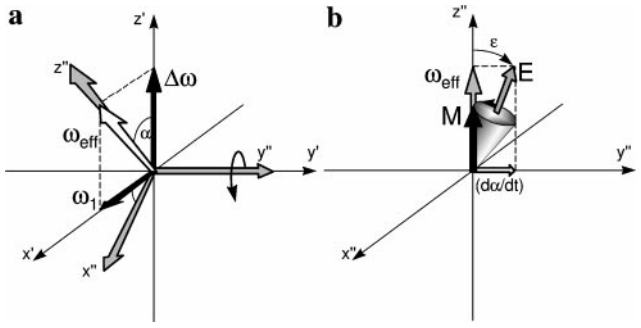

FIG. 5. Vector diagrams showing the effective field and its components in two rotating frames of reference. (a) Relationship between the $\omega_{\rm RF}$ frame (x', y', z') and the $\omega_{\rm eff}$ frame (x'', y'', x''). (b) Magnetic field components and evolution of the magnetization vector (**M**) in the $\omega_{\rm eff}$ frame.

amplitude ($\omega_1^{\rm max}$), which is the basis for their highly touted "B_1 insensitivity." However, the vector depiction in the $\omega_{\rm RF}$ frame as given in the previous section does not explain why **M** follows $\boldsymbol{\omega}_{\mathbf{eff}}(t)$ during an adiabatic passage. For this purpose, it is necessary to define a second frame of reference which rotates with $\boldsymbol{\omega}_{\mathbf{eff}}(t)$, called the "$\omega_{\rm eff}$ frame." In the $\omega_{\rm eff}$ frame, the origin of the adiabatic condition can be made readily apparent.

Figure 5a depicts the relationships between the $\omega_{\rm RF}$ and $\omega_{\rm eff}$ frames during an adiabatic passage. The axes of the $\omega_{\rm eff}$ frame are labeled with double primes, x'', y'', z''. Initially, the two frames are superimposed. As the adiabatic passage proceeds, the $\omega_{\rm eff}$ frame rotates about y' ($=y''$) with an instantaneous angular velocity $d\alpha/dt$, while $\boldsymbol{\omega}_{\mathbf{eff}}$ remains collinear with z''. By the end of the pulse, the two frames are related by an angle (=flip angle) which is determined by the extent of the $\boldsymbol{\omega}_{\mathbf{eff}}$ sweep.

Figure 5b shows the relationships between **M** and the magnetic field components in the $\omega_{\rm eff}$ frame. The rotation of the $\omega_{\rm eff}$ frame about y' gives rise to a fictitious field component along y'', which has an instantaneous magnitude equal to $d\alpha/dt$. Thus, in the $\omega_{\rm eff}$ frame, the effective magnetic field $\mathbf{E}(t)$ is the vector sum of $\boldsymbol{\omega}_{\mathbf{eff}}(t)$ and $(d\alpha/dt)\hat{\mathbf{y}}''$. To simplify the picture, let us choose a pair of modulation functions, $\omega_1(t)$ and $\Delta\omega(t)$, such that $\omega_{\rm eff}$ and $d\alpha/dt$ are constants for the duration of the adiabatic passage. In this case, **M** simply evolves about **E** on the cone of angle ε. As shown in Fig. 5b, **M** never strays beyond an angle 2ε from $\boldsymbol{\omega}_{\mathbf{eff}}$. When the adiabatic condition given by Eq. [11] is well satisfied, ε is small, and thus, the motion of **M** closely traces the trajectory of $\boldsymbol{\omega}_{\mathbf{eff}}(t)$ in the $\omega_{\rm RF}$ frame.

Likewise, for components of **M** that are initially perpendicular to $\boldsymbol{\omega}_{\mathbf{eff}}$, the angle between $\boldsymbol{\omega}_{\mathbf{eff}}(t)$ and **M** remains within $90^\circ \pm \varepsilon$. Thus, **M** stays approximately perpendicular to $\boldsymbol{\omega}_{\mathbf{eff}}(t)$ when the adiabatic condition is well satisfied. This principle is exploited in the adiabatic plane rotation pulses described in Section IV.

The analysis in the $\omega_{\rm eff}$ frame above isolates the perturbation (i.e., $[d\alpha/dt]\hat{\mathbf{y}}''$) that must be minimized to achieve the desired rotation with an adiabatic pulse and explains the origin of the adiabatic condition (Eq. [11]). It is also noted that the $\omega_{\rm eff}$ frame is a useful platform to visualize the behavior of adiabatic and other types of pulses. As discussed in Section IV, adiabatic plane rotation pulses function by forming an echo in the $\omega_{\rm eff}$ frame in a manner similar to a rotary echo (*61*), except the adiabatic echo is formed by inverting $\boldsymbol{\omega}_{\mathbf{eff}}$ instead of $\boldsymbol{\omega}_{\mathbf{1}}$.

The $\omega_{\rm eff}$ frame can also facilitate the design of new types of pulses (adiabatic or otherwise). To demonstrate this latter point, consider the possibility of rotating **M** from z'' to y'' about the effective field **E** in the $\omega_{\rm eff}$ frame. Because y'' and y' represent the same axis, this process yields a 90° excitation in the $\omega_{\rm RF}$ frame (x', y', z') and in the $\omega_{\rm eff}$ frame (x'', y'', z''). The most straightforward way to achieve this rotation is to employ constant and equal amplitudes for the field components in the $\omega_{\rm eff}$ frame (i.e., $\omega_{\rm eff} = d\alpha/dt = \text{constant}$), so that **E** remains fixed in the $y''z''$ plane at a 45° angle relative to z''. With AM and FM functions based on sine and cosine functions with the same amplitudes, this requirement for constant $\omega_{\rm eff}$ and $d\alpha/dt$ can be satisfied. By setting the proper pulse length, a rotation of 180° about **E** takes **M** from z'' to y'' ($=y''$). Figure 6 shows the modulation functions of this FM pulse and the excitation profile in the $\omega_{\rm RF}$ frame as predicted by the Bloch equation. For comparison, Fig. 6 also shows the simulated excitation profile of a square pulse. Both pulses require the same ω_1 intensity ($\omega_1^{\rm max}/2\pi = 2.5$ kHz). Interestingly, the excitation bandwidth of the FM pulse comes close to that of a square 90° pulse, which is one of the best pulses for compensating errors caused by resonance offset.

III. OPTIMIZATION OF MODULATION FUNCTIONS

IIIA. Adiabaticity

Many different functions have been proposed to drive the amplitude and frequency modulations of adiabatic pulses (*4, 5, 7, 8, 10–15, 19, 25, 37, 47, 54, 57, 60, 62–74*). For more than a decade, considerable effort was focused on the design of modulation functions which maximize the inequality of the adiabatic condition (Eq. [11]). Many of the previously proposed modulation functions were derived from theoretical analyses considering only the center isochromat ($\Omega = 0$); consequently, the efficiency of these pulses generally degrades as the resonance offset increases.

An extraordinary property of the HS1 (or sech/tanh) pulse is its insensitivity to increases in $\omega_1^{\rm max}$ beyond the threshold value needed to sufficiently satisfy the adiabatic condition. With the HS1 pulse, the magnitude of the longitudinal magnetization (M_z) is essentially uniform inside the distinct borders governed by the limits of the frequency sweep. The latter feature is a consequence of the fact that the adiabaticity is invariant when $\boldsymbol{\omega}_{\mathbf{eff}}(t)$ crosses the $x'y'$ plane for all isochromats in the sweep range, $-A < \Omega < A$ (*12, 13*). In Section IIIB, we present methods used to generate arbitrary pulse shapes with this property that we call offset-independent adiabaticity (OIA).

With any set of modulations functions, the trajectory of $\boldsymbol{\omega}_{\mathbf{eff}}(t)$, as well as the time at which the adiabatic condition is most likely to be violated, are functions of the experimental

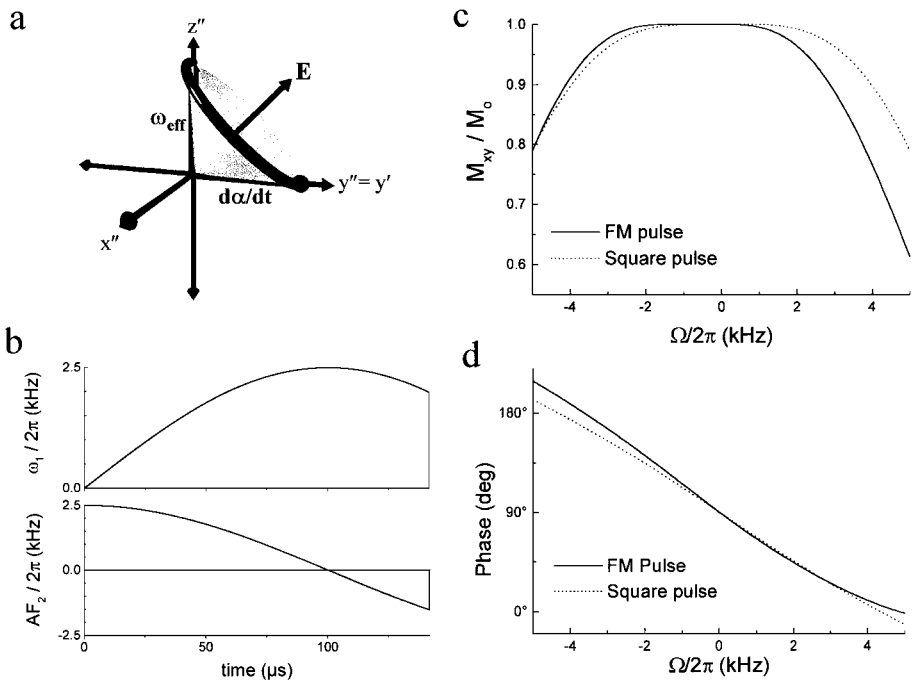

FIG. 6. A pulse that has AM and FM functions based on sine and cosine functions with equal amplitudes. (a) With this choice of modulation functions and by properly setting the pulse length, the pulse can produce a 180° rotation about the effective field **E** in the ω_{eff} frame, which is equivalent to a net rotation of 90° in the ω_{RF} frame. (b) Amplitude ($\omega_1/2\pi$) and frequency ($AF_2/2\pi$) modulations used for the FM pulse. (c) Comparison of the normalized excitation profiles (M_{xy}/M_0) produced by the FM pulse (solid line) versus a conventional square pulse (dashed line). The FM pulse was 41% longer than the square pulse, but produced 88% of the bandwidth at $M_{xy}/M_0 = 0.8$ with 86% of the energy used by the square pulse. (d) Phase profiles of the M_{xy} produced by the FM and square pulses.

variables $\omega_1^{\max}$ and Ω. A procedure known as the numerically optimized modulation (NOM) method offers the possibility to obtain driving functions which yield optimal adiabaticity across a specified range of $\omega_1^{\max}$ and/or Ω values (*7*, *64*, *67*). By this latter approach, the time-dependence of the AM and FM functions is distorted to ensure that the level of adiabaticity (across the desired range of $\omega_1^{\max}$ and Ω values) does not fall below a certain threshold level at any time during the pulse. The NOM procedure is described in Section IIIC.

With either optimization procedure (OIA or NOM), the adiabatic condition must be expressed as a ratio K, with explicit dependence on the variables $\omega_1^{\max}$, Ω, and t. Accordingly, for the time interval equal to the pulse duration T_{p} and for the offset interval $|\Omega| < A$, the adiabatic condition is expressed as a ratio

$$K\left(\omega_1^{\max}, \Omega, t\right) = \left|\frac{\omega_{\text{eff}}\left(\omega_1^{\max}, \Omega, t\right)}{\dot{\alpha}}\right| = \frac{A^2}{\omega_1^{\max}} \frac{\left[\left(\omega_1^{\max} F_1(t)/A\right)^2 + \left[F_2(t) - \Omega/A\right]^2\right]^{\frac{3}{2}}}{\left|(F_2(t) - \Omega/A)\dot{F}_1(t) - F_1(t)\dot{F}_2(t)\right|} \gg 1, \quad [15]$$

where $\dot{\alpha}$ is the rate of change of the orientation of $\boldsymbol{\omega}_{\text{eff}}(t)$. The functions $F_1(t)$ and $F_2(t)$ describe the shapes of the AM and FM envelops, which are dimensionlesss and have values in the range 0 to 1 and -1 to 1, respectively. In the following sections, we describe two different ways to tailor and optimize $F_1(t)$ and $F_2(t)$ to satisfy different experimental requirements and conditions.

IIIB. Offset-Independent Adiabaticity (OIA)

With conventional pulses (e.g., AM only pulses), approximately equal amounts of RF energy are delivered to every isochromat in the bandwidth at any given time during the pulse. In the method used here, an equal amount of RF energy is applied to all isochromats, but this energy is distributed sequentially in time over the bandwidth (*62*). Accordingly, the principle of OIA requires $K(\omega_1^{\max}, \Omega, t)$ to be equally satisfied for all values of Ω inside the frequency sweep bandwidth (*BW*).

With most reasonable choices for the driving functions $F_1(t)$ and $F_2(t)$, the adiabatic factor K is smallest at the time when resonance condition is achieved (i.e., when $AF_2(t_\Omega) = \Omega$). At this time t_Ω, $\boldsymbol{\omega}_{\text{eff}}$ lies on the $x'y'$ plane, and thus, $\omega_{\text{eff}}(t_\Omega) \leq \omega_1^{\max}$. Obviously, the maximum allowable value of $\omega_1^{\max}$ is subject to experimental constraints, and in many cases, it is desirable to accomplish the task using the lowest possible $\omega_1^{\max}$. OIA pulses provide the same degree of adiabaticity for the different isochromats in the range $-A < \Omega < A$ at that critical time t_Ω when the effective field crosses the transverse plane.

To derive the formula for offset-independent adiabaticity, the adiabaticity equation (Eq. [15]) is simplified by noting that at

times $t = t_\Omega$,

$$F_2(t_\Omega) = \Omega/A. \quad [16]$$

Substitution of Eq. [16] into Eq. [15] yields

$$K(t_\Omega) = \frac{\left(\omega_1^{\max} F_1(t_\Omega)\right)^2}{A\dot{F}_2(t_\Omega)}. \quad [17]$$

Hence the identity

$$K(t_\Omega)A\dot{F}_2(t_\Omega) = \left(\omega_1^{\max} F_1(t_\Omega)\right)^2 \quad [18]$$

specifies the relationship between the two driving functions, $F_1(t)$ and $F_2(t)$. It states that, for all isochromats with $|\Omega| < A$, $(\omega_1^{\max} F_1(t_\Omega))^2$ must be greater than the rate of change of the frequency sweep $A\dot{F}_2(t_\Omega)$ *by the same factor* $K(t_\Omega)$. Equation [18] can thus be used to calculate pairs of AM and FM functions which yield constant $K(t_\Omega)$ for all isochromats. In other words, any pair of modulation functions that can satisfy Eq. [18] will achieve uniform adiabaticity as $AF_2(t)$ sweeps through resonance for all values of Ω in the sweep range.

Table 1 lists several examples of OIA inversion pulses that conform to the OIA equation (Eq. [18]). The results shown were obtained by numerical simulation of the Bloch equation using $A/2\pi = 25$ kHz and $T_p = 2$ ms. Performance parameters that are compared include: *i*) the minimum value of $\omega_1^{\max}$ that is needed to perform 99% inversion ($M_z/M_0 \leq -0.98$) at the center of the bandwidth; *ii*) ω_1^{rms}, the root mean square (rms) of the amplitude modulation, and *iii*) the inversion profile quality factor, $Q \equiv 2\pi BW_{90\%}/\omega_1^{\text{rms}}$, where $BW_{90\%}$ is the bandwidth in which $M_z/M_0 \leq -0.80$. Although the parameters chosen for the pulses in Table 1 were selected for broadband applications, both BW and $\omega_1^{\max}$ scale inversely with T_p, while the performance factor Q remains unchanged. Notice that all pulses listed in Table 1 require approximately the same ω_1^{rms} value. Also note that pulses with the flattest AM functions perform rotations with the lowest $\omega_1^{\max}$ values, since the RF energy is distributed more evenly in time. The ideal AM shapes approach that of the chirp pulse, but with smooth transitions to zero at the extremities. Based on this logic, we have developed a class of flattened HS1 pulses using a non-linear argument, $\eta(\tau) = \beta\tau^n$ (instead of $\beta\tau$) in the driving functions, where τ denotes normalized time (i.e., $\tau = 2t/T_p - 1$, for t in the range $[0, T_p]$). With these latter pulses, called HSn pulses, the smoothness of the transition at the extremities of the AM function can easily be tuned by adjusting the parameter n (*13*). Similar AM shapes can be generated by stretching known adiabatic pulses (*11*), as well as by using the NOM procedure described in the next section. Although not discussed here, highly efficient OIA pulses for applications requiring spatially-selective inversion (e.g., in MRI experiments) can be generated using an extension of the OIA formalism that accommodates a time-dependent B_0 gradient (*74*).

TABLE 1
Modulation Functions and Performance Comparison of Some OIA Inversion Pulses[a]

Pulse	$F_1(\tau)$	$F_2(\tau)$	$\omega_1^{\max}/2\pi$[b] (kHz)	$\omega_1^{\text{rms}}/2\pi$[c] (kHz)	Q[d]
Lorentz	$\frac{1}{1+\beta\tau^2}$	$\frac{\tau}{1+\beta\tau^2} + \frac{1}{\sqrt{\beta}}\tan^{-1}(\sqrt{\beta}\tau)$	11.49	3.25	15.08
HS1	$\text{sech}(\beta\tau)$	$\frac{\tanh(\beta\tau)}{\tanh(\beta)}$	7.56	3.28	14.81
Gauss	$\exp\left(-\frac{\beta^2\tau^2}{2}\right)$	$\frac{\text{erf}(\beta\tau)}{\text{erf}(\beta)}$	6.13	3.29	14.67
HS8[e]	$\text{sech}(\beta\tau^n)$	$\int \text{sech}^2(\beta\tau^n)\,d\tau$	3.71	3.25	14.49
chirp	1	τ	3.38	3.38	11.24

[a] The performance parameters, $\omega_1^{\max}$, ω_1^{rms}, and Q, were determined from simulations using $A/2\pi = 25$ kHz and $T_p = 2$ms.

[b] $\omega_1^{\max}$ is the minimum value that produces at least 99% inversion ($M_z/M_0 \leq -0.98$).

[c] ω_1^{rms} is the root mean square value of $\omega_1(t)$.

[d] Q is a quality factor defined as $2\pi BW_{90\%}/\omega_1^{\text{rms}}$, where $BW_{90\%}$ is the bandwidth for better than 90% inversion ($M_z/M_0 \leq -0.80$).

[e] $n = 8$; $F_2(\tau)$ must be obtained by numerical integration of $F_1(\tau)^2$; $|\tau| \leq 2t/T_p$.

To further illustrate the features of offset-independent adiabaticity, Eq. [15] was used to ascertain the dependence of K on the variables Ω and τ. Figure 7 shows plots of $K(\Omega, \tau)$ for four different pairs of modulation functions, all using $T_p = 2$ ms, $A/2\pi = 5$ kHz, and the threshold value of $\omega_1^{\max}$ that induces 99% inversion ($M_z/M_0 \leq -0.98$) at $\Omega = 0$ with each pulse type. To indicate the time t_Ω that each isochromat reaches resonance, the FM function of each pulse is overlaid on each plot (dashed line). As predicted, K is the same at all t_Ω with HS1 and HS8 (Figs. 7a and 7b, respectively). Upon close inspection, however, it can be seen that the adiabaticity drops slightly in regions immediately adjacent to the $AF_2(t)$ curves at the extreme times, and this phenomenon is most prominent in HS8 (Fig. 7b). As expected, such minor differences in the adiabaticity are reflected in the M_z/M_0 profiles of these pulses, as shown in Figs. 8 and 9. The advantage of HS8 over HS1, however, is its ability to perform the transformation with considerably less peak RF power (i.e., to achieve 99% inversion with these HS1 and HS8 pulses, $\omega_1^{\max}/2\pi = 3.34$ and 1.8 kHz, respectively).

As illustrated in Fig. 7, the OIA method ensures that the adiabaticity is uniform for all isochromats at time t_Ω, but provides no way to control the adiabaticity at other times. As described in the next section, the NOM method provides a way to avoid dropping below a specified minimum adiabaticity at any time during the pulse.

IIIC. Numerical Optimization of the Adiabatic Condition (NOM)

Obviously, it is not possible to analytically solve Eq. [15] to obtain a unique pair of modulation functions that satisfy the adiabatic condition at all times. However, solutions to this problem can be found by selecting some initial F_1 and F_2 functions and

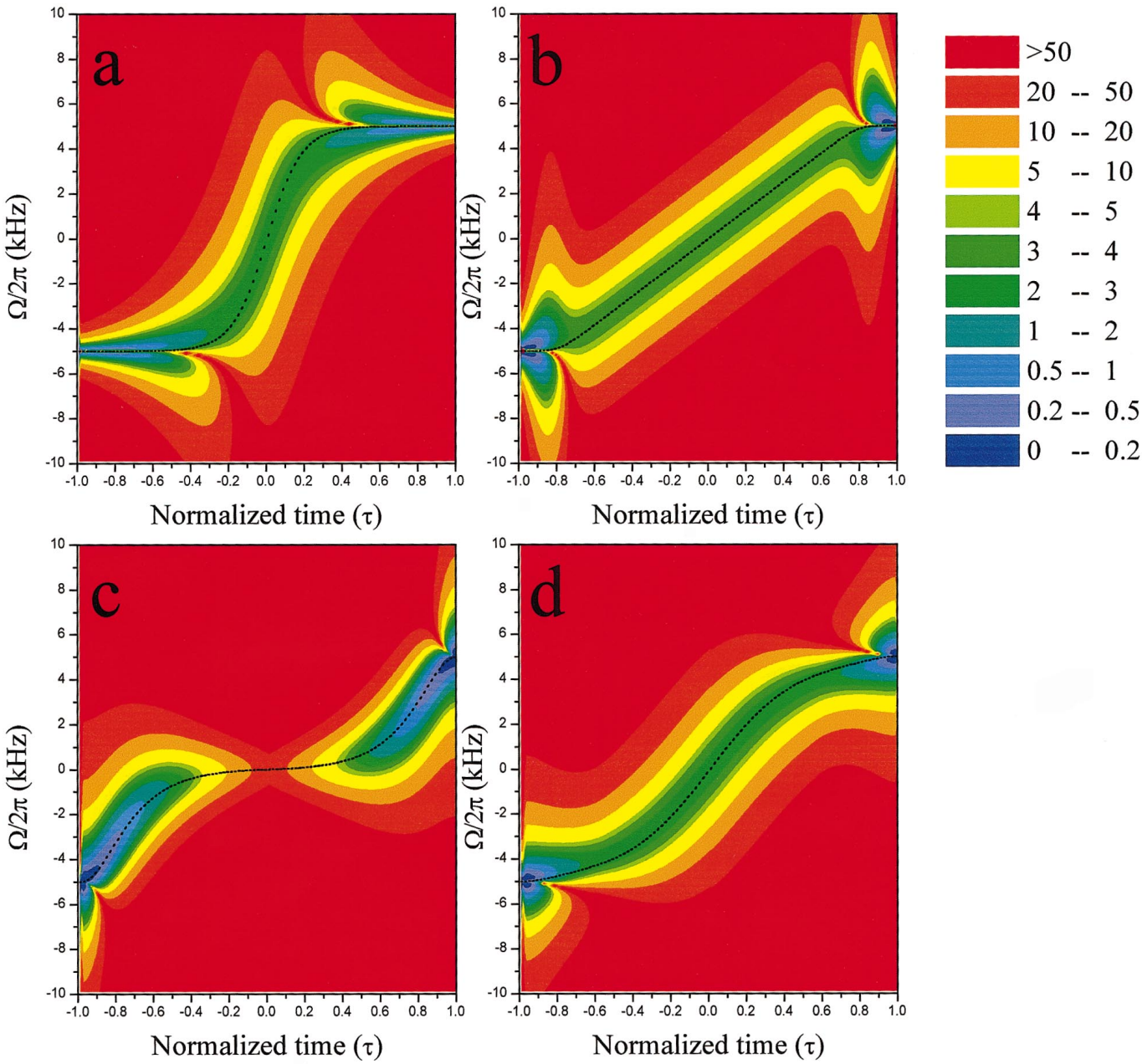

FIG. 7. Plots of adiabaticity (K) as functions of resonance offset (Ω) and normalized time (τ). (a) HS1 using $\omega_1^{\max}/2\pi = 3.34$ kHz, (b) HS8 using $\omega_1^{\max}/2\pi = 1.8$ kHz, (c) tanh/sech using $\omega_1^{\max}/2\pi = 1.2$ kHz, and (d) a NOM version of tanh/sech using $\omega_1^{\max}/2\pi = 2.12$ kHz. Other pulse parameters were $A/2\pi = 5$ kHz and $T_p = 2$ ms.

then driving them with an unspecified function $\eta(t)$ which is non-linear in time. Accordingly, Eq. [15] becomes

$$K\left(\omega_1^{\max}, \Omega, t\right) = \frac{A^2}{\omega_1^{\max}} \frac{\left[\left(\omega_1^{\max} F_1(\eta)/A\right)^2 + \left[F_2(\eta) - \Omega/A\right]^2\right]^{\frac{3}{2}}}{\left|\left[(F_2(\eta) - \Omega/A)\dot{F}_1(\eta) - F_1(\eta)\dot{F}_2(\eta)\right](\dot{\eta}(t))\right|} \gg 1. \quad [19]$$

In the NOM procedure, the goal is then to find the $\eta(t)$ function, for the range of $\omega_1^{\max}$ and Ω values of interest, which keeps the adiabaticity from falling below a certain value γ_0 at any time during the pulse. This requirement can be expressed as

$$K\left(\omega_1^{\max}, \Omega, t\right) \geq \gamma_0. \quad [20]$$

Upon combining Eqs. [19] and [20] and re-arranging terms,

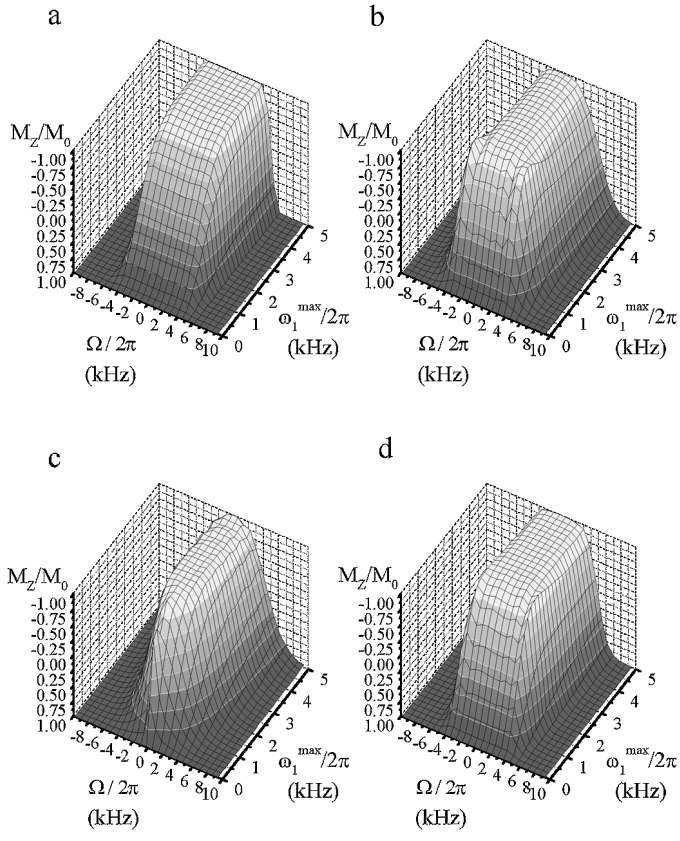

FIG. 8. Theoretical inversion profiles (M_z/M_0) as functions of resonance offset (Ω) and RF amplitude (ω_1^{max}), as produced by (a) HS1, (b) HS8, (c) tanh/sech, and (d) a NOM version of tanh/sech. Pulse parameters were $A/2\pi = 5$ kHz and $T_p = 2$ ms.

we have

$$\dot{\eta}(t) \le \frac{f\left(\omega_1^{\max}, \Omega, t\right)}{\gamma_0}, \qquad [21]$$

where

$$f\left(\omega_1^{\max}, \Omega, t\right) \equiv \frac{A^2}{\omega_1^{\max}} \frac{\left[\left(\omega_1^{\max} F_1(\eta)/A\right)^2 + [F_2(\eta) - \Omega/A]^2\right]^{\frac{3}{2}}}{|[(F_2(\eta) - \Omega/A)\dot{F}_1(\eta) - F_1(\eta)\dot{F}_2(\eta)]|}. \qquad [22]$$

For each value of η, there is a unique set of $\omega_1^{\max}$ and Ω values at which $f(\omega_1^{\max}, \Omega, t)$ achieves a minimum value $f_{\min}(\eta)$. If the $\dot{\eta}(t)$ at each η is set equal to this minimum value, then the condition set by Eq. [21] will be fulfilled over the range of $\omega_1^{\max}$ and Ω values of interest. Equating $\dot{\eta}(t)$ with $f_{\min}(\eta)$ defines the time derivative of $\eta(t)$ as a function of η itself,

$$\dot{\eta}(t) = \frac{d}{dt}\eta(t) = \frac{f_{\min}(\eta)}{\gamma_0}. \qquad [23]$$

Integration of Eq. [23] yields

$$t(\eta) = \gamma_0 \int_0^{\eta} d\eta' [\, f_{\min}(\eta')]^{-1}. \qquad [24]$$

This integral can be solved numerically to obtain a set of η values and the corresponding t values. Numerical interpolation on this data set then yields the desired function, $\eta(t)$, which is then used to drive F_1 and F_2 in the optimized pulse. Because $\eta(t)$ is constructed numerically, we refer to the modulation functions obtained by this procedure as NOM (numerically optimized modulation). Obviously, this numerical procedure is distinctly different from iterative minimization algorithms which have been used to optimize composite and other types of pulses (*75*).

By showing some examples, the strength of the NOM procedure becomes readily apparent. As stated above, the first step in the process is to make an initial choice for the modulation functions, F_1 and F_2. For demonstration purposes, we begin by interchanging the modulation functions normally used for HS1. Specifically, the functions used are

$$F_1(t) = \tanh(2\beta t/T_p) \quad (0 < t < 0.5T_p) \qquad [25]$$

$$F_1(t) = \tanh(2\beta(1 - t/T_p)) \quad (0.5T_p < t < T_p) \qquad [26]$$

$$F_2(t) = \frac{\operatorname{sech}(\beta) - \operatorname{sech}(2\beta t/T_p)}{1 - \operatorname{sech}(\beta)} \quad (0 < t < 0.5T_p) \qquad [27]$$

$$F_2(t) = \frac{\operatorname{sech}(2\beta(1 - t/T_p)) - \operatorname{sech}(\beta)}{1 - \operatorname{sech}(\beta)} \quad (0.5T_p < t < T_p) \qquad [28]$$

Other parameters in this tanh/sech pulse are identical to those used for the OIA pulses in Section IIIB, except $\omega_1^{\max}/2\pi = 2.12$ kHz, which is the threshold value determined from simulations to produce 99% inversion at the center of the bandwidth of this pulse. Figure 7c shows the adiabaticity (K) of the tanh/sech pulse as a function of Ω and τ. By following along the FM function that is overlaid on the plot, it is apparent that the adiabaticity at t_Ω varies for different isochromats. The adiabaticity is greatest for isochromats that reach resonance close to the midpoint of the pulse. As expected, this pulse inverts the isochromat at the center of the frequency sweep with a relatively low $\omega_1^{\max}$ value, but the degree of inversion quickly diminishes on either side of $\Omega = 0$, as shown in Fig. 8c.

The NOM procedure was performed on the tanh/sech pulse over the range -4 kHz $\le \Omega \le 4$ kHz, while $\omega_1^{\max}/2\pi$ was fixed at 2.12 kHz. As Figs. 7d and 8d show, the NOM procedure successfully transformed this tanh/sech pulse into a pulse with highly competitive features. With the NOM pulse, the minimum adiabaticity is uniform for all isochromats in the bandwidth specified for the optimization (Fig. 7d). Furthermore, the superior qualities of the inversion profile produced by this NOM pulse (Fig. 8d)

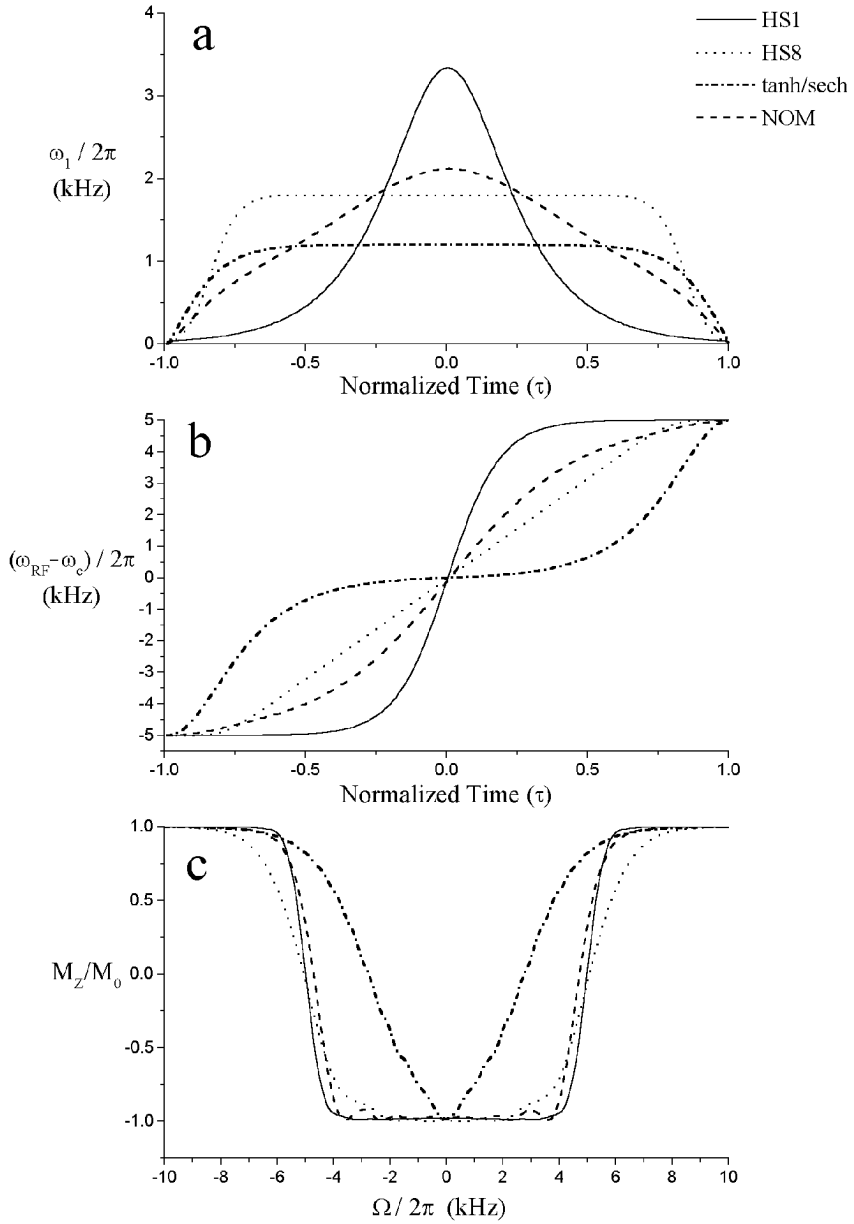

FIG. 9. (a) AM and (b) FM functions, and (c) inversion profiles of the four pulses, HS1, HS8, tanh/sech, and a NOM version of tanh/sech. Inversion profiles in (c) were calculated using $A/2\pi = 5$ kHz and $T_p = 2$ ms.

approach those of the HS1 pulse (Fig. 8a), while doing so with considerably less peak RF power. These features can be seen more clearly in Fig. 9, which shows the AM and FM functions and the corresponding inversion profiles produced by the four pulses considered so far.

Although the optimization above was performed allowing only a single parameter (Ω) to vary, the optimization can also be performed over a predefined range of multiple variables (e.g., ω_1^{max} and Ω, simultaneously). For example, we previously performed the NOM procedure on the tanh/sech pulse over the range $-0.33 < \Omega/A < 0.33$ and $\omega_1^{max}/A = 0.02$ to 1 (67). To describe the resultant NOM pulse analytically, it can be approximated by the tanh/tan functions,

$$\omega_1(t) = \omega_1^{max} \tanh\left(\frac{2\xi t}{T_p}\right) \quad (0 < t < 0.5T_p) \qquad [29]$$

$$\omega_1(t) = \omega_1^{max} \tanh\left(2\xi\left(1 - \frac{t}{T_p}\right)\right) \quad (0.5T_p < t < T_p) \qquad [30]$$

$$\omega_{\mathrm{RF}}(t) - \omega_{\mathrm{c}} = A\left(\frac{\tan(\kappa(2t/T_{\mathrm{p}} - 1))}{\tan(\kappa)}\right), \quad (0 < t < T_{\mathrm{p}}) \quad [31]$$

with constants $\xi = 10$, $\kappa = \arctan[18]$, and $R = 40$ ($\equiv AT_{\mathrm{p}}/\pi$). This tanh/tan AFP pulse is well suited for the purpose of inverting spins rapidly in experiments that do not require a sharp transition between inverted and non-inverted spectral regions. With this pulse, the inversion bandwidth is limited by the ability to satisfy the adiabatic condition off resonance, not the extent of the sweep range, which by design is much wider than operational bandwidth. With low $\omega_1^{\max}$ values, the adiabatic condition can be sufficiently satisfied only for isochromats with Larmor frequencies near the center of the frequency sweep range, since the sweep rate accelerates very rapidly in either direction away from the center of the pulse.

To further highlight the features of different modulation functions, two of the common conventional pulse types (square and sinc-shaped pulses) were compared with tanh/tan and HS1 pulses using Bloch simulations. In each case, pulse parameters were set to produce a 5 kHz bandwidth (fwhm). The $\omega_1^{\max}$ value of each pulse was adjusted to produce 95% inversion ($M_z/M_0 = -0.9$) at the center of its inversion profile. Of interest are the resultant values of $\omega_1^{\max}$, T_{p}, and the relative RF energy (E_{rel}) used with each pulse (Table 2). For example, at the threshold value of $\omega_1^{\max}$ where the tanh/tan pulse achieves satisfactory inversion ($M_z/M_0 \leq -0.9$), the required RF energy is nearly identical to that needed to produce the same degree of inversion and bandwidth with an ordinary square pulse. However, the square pulse requires $\omega_1^{\max}$ to be almost twofold greater than that required by the tanh/tan pulse, whereas the duration of the tanh/tan pulse is fourfold longer than the square pulse. Like most AFPs, for a range of $\omega_1^{\max}$ values above the threshold value needed to achieve adiabaticity, the tanh/tan pulse continues to produce complete inversion ($M_z/M_0 \approx -1$). Of course the inversion produced with the conventional pulse is proportional to $\cos(\omega_1^{\max} T_{\mathrm{p}})$. Thus, for many applications that require nonselective spin inversion, it may be preferable to use the tanh/tan pulse instead of the square pulse since the RF energy deposited is the same (when using the minimum $\omega_1^{\max}$ value needed to achieve inversion with the adiabatic pulse) and the adiabatic pulse has the additional feature of continuing to produce inversion in spatial locations that experience a larger $\omega_1^{\max}$ value (e.g., in the regions closest to the RF coil).

TABLE 2
Performance Comparison of Different Pulses Used for Inversion

Pulse [a]	T_{p} (ms)	$\omega_1^{\max}/2\pi$ (kHz)	E_{rel}^{b}
180° square	0.16	2.68	1
tanh/tan ($R = 40$)	0.64	1.41	1
180° sinc	0.94	2.57	0.87
HS1 ($R = 20$)	4.0	1.35	1.20

[a] For all pulses, $BW(\mathrm{fwhm}) = 5$ kHz.

[b] Relative RF energy, $E_{\mathrm{rel}} \propto \int_0^{T_{\mathrm{p}}} \omega_1^2(t)\,dt$.

IV. ADIABATIC PLANE ROTATION PULSES

IVA. A Need for the All Purpose Adiabatic Pulse

As mentioned earlier, the classical adiabatic passage offers only limited utility in contemporary NMR, since **M** must be moved from point to point in alignment with the sweeping effective field, $\boldsymbol{\omega}_{\mathbf{eff}}(t)$. For this reason, an AFP can induce population inversion, but is not a suitable refocusing pulse for spin-echo generation.

The limited versatility of the classical adiabatic passage created a need for a general purpose adiabatic pulse that can convert all initial states of **M** into the final states that would result after an ideal pulse. *Composite* adiabatic pulses are the product of research which sought to develop such pulses. The first adiabatic pulses to accomplish this task belong to a class of pulses known as B_1-insensitive rotation (BIR) pulses (*47–50, 52, 54*). Two of the most versatile BIR pulses are shown in Fig. 10. These BIR pulses have the ability to generate a uniform flip angle for all components of **M** that lie perpendicular to the rotation axis. The flip angle can be any arbitrary value and is determined by one or more phase shifts ($\Delta\phi$) that take place at specific times during the pulse. As shown in Fig. 10, these composite adiabatic pulses are constructed from two fundamental segments: an AHP (Fig. 10a) and its inverse (Fig. 10b). The first generation plane rotation pulse known as BIR-1 (Fig. 10c) lacks compensation for resonance offset ($\Omega \neq 0$). However, the pulse known as BIR-4 (Fig 10d) can rotate magnetization vectors about an axis that can be highly invariant to resonance offsets in the range $|\Omega| < A$. In this section, we provide a theoretical framework to analyze and derive such pulses.

IVB. Vector Description of BIR Pulses

Although BIR-1 is not compensated for resonance offset, for the sake of simplicity we begin with a vector description of BIR-1 for the case of $\Omega = 0$. The motions of $\boldsymbol{\omega}_{\mathbf{eff}}$ and **M** during a 90° BIR-1 of length T_{p} are shown in the ω_{RF} frame in Figs. 11a–d. At the beginning of BIR-1, ω_{RF} is applied on resonance ($\Delta\omega(0) = 0$). Thus, unlike the classical adiabatic passage described in Section II, initially $\boldsymbol{\omega}_{\mathbf{eff}}$ lies on the transverse plane (i.e., $\alpha(0) = 90°$) and is perpendicular to the equilibrium magnetization, $\mathbf{M_0}$. A vector analysis similar to that performed in Section II can be used to prove that the angle between $\boldsymbol{\omega}_{\mathbf{eff}}$ and **M** will remain between $90° - \varepsilon$ and $90° + \varepsilon$ during the pulse. To simplify the problem, here we assume that the adiabatic condition is well satisfied ($\omega_{\mathrm{eff}}(t) \gg |d\alpha/dt|$), so that ε can be set to zero.

In this analysis, the initial phase of $\boldsymbol{\omega}_{\mathbf{1}}$ is arbitrarily chosen to coincide with x' (Fig. 11a). During the first half of BIR-1, $\boldsymbol{\omega}_{\mathbf{eff}}$ sweeps from x' to z', while **M** rotates about $\boldsymbol{\omega}_{\mathbf{eff}}$ (Figs. 11a–b). At $t = T_{\mathrm{p}}/2$, the orientation of **M** can be obtained from the solution of the Bloch equation,

$$\frac{d\mathbf{M}}{dt} = \mathbf{M} \times \boldsymbol{\omega}_{\mathbf{eff}} = \mathbf{M} \times \frac{d\Psi}{dt}, \quad [32]$$

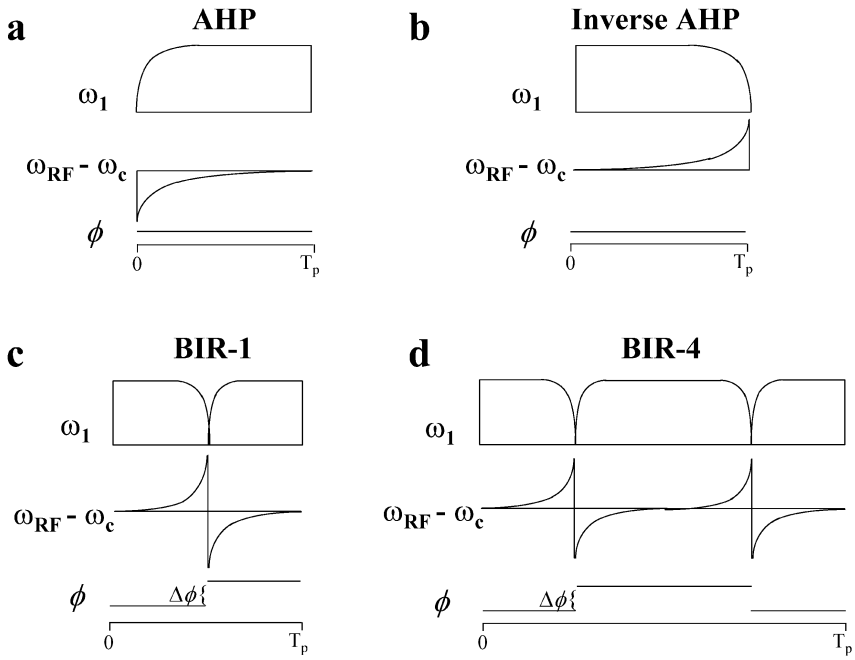

FIG. 10. AM, FM, and phase (ϕ) functions for (a) the adiabatic half-passage, (b) the inverse adiabatic half-passage, and the adiabatic plane rotation pulses, (c) BIR-1 and (d) BIR-4.

where $d\Psi/dt$ is the rate of change of **M** around $\boldsymbol{\omega_{eff}}$ since the equation has the form of the angular momentum precession equation (*4*). Provided that the adiabatic condition is satisfied throughout the first segment of the pulse, **M** is in the $x'y'$ plane at $t = T_p/2$ and the accumulated evolution angle (ψ) about $\boldsymbol{\omega_{eff}}$ at this time is simply

$$\psi(T_p/2) = \int_0^{T_p/2} \omega_{\text{eff}}(t)\, dt. \qquad [33]$$

By this point in time ($t = T_p/2$), a time-reversed AHP has been completed. At this halfway point, the orientation of $\boldsymbol{\omega_{eff}}$ is instantaneously inverted by jumping the modulation frequency from A to $-A$, and the second half of the pulse is simply a normal AHP using AM and FM functions which are mirror images of those used for the first half. To produce the desired flip angle θ, the phase of $\boldsymbol{\omega_1}$ used in the second half of the pulse is shifted relative to the first half by $\Delta\phi = 180^\circ + \theta$. Accordingly, $\boldsymbol{\omega_{eff}}$ sweeps from $-z'$ to $-y'$ during the second half of 90° BIR-1 (Figs. 11c–d).

In the ω_{eff} frame, **M** rotates about x'' in opposite directions during the first and second halves of the pulse, so that the net evolution angle ψ for the total pulse is zero. Thus, the central $\boldsymbol{\omega_{eff}}$ flip, together with the subsequent time reversal of the modulation functions, compensate (refocus) the evolution which took place during the first and second halves of the pulse (i.e., $\psi_{\text{tot}} = 0$). This phenomenon is equivalent to a rotary echo (*61*) in the ω_{eff} frame.

The $\Delta\phi$ phase shift between the first and second segments of BIR-1 determines the flip angle and the final orientation of the ω_{eff} frame relative to the ω_{RF} frame. In 90° BIR-1 (Figs. 11a–d), the transformation of the ω_{eff} frame in relation to the ω_{RF} frame is equivalent to a -90° rotation about y' followed by a -90° rotation about x'. In the ω_{RF} frame, the net rotation of **M** is equivalent to a -90° rotation about x', followed by a 90° rotation (phase shift) about z'. It is also possible to show that BIR-1 can induce any flip angle by setting $\Delta\phi = 180^\circ + \theta$, in which case the net rotation of **M** is equivalent to a $-\theta$ rotation about x', followed by a phase shift of θ about z'. Although Fig. 11 shows only the vector motions for the initial condition of **M** along z', the plane rotation properties of the pulse can be revealed by performing similar vector analyses with **M** having other initial orientations.

In the presence of a resonance offset Ω ($=\omega_0 - \omega_c \neq 0$), the performance of BIR-1 degrades for two reasons. First, a rotary echo in the ω_{eff} frame may not be achieved, since the net evolution of **M** about $\boldsymbol{\omega_{eff}}$ depends on Ω according to

$$\psi_{tot} = -\int_0^{T_p/2} \sqrt{(\omega_1(t))^2 + (\Omega - AF_2(t))^2}\, dt + \int_{T_{p/2}}^{T_p} \sqrt{(\omega_1(t))^2 + (\Omega - AF_2(t))^2}\, dt, \qquad [34]$$

where the two terms describe the evolution angles in the first and second halves of BIR-1, respectively. When $\Omega \neq 0$, the first and

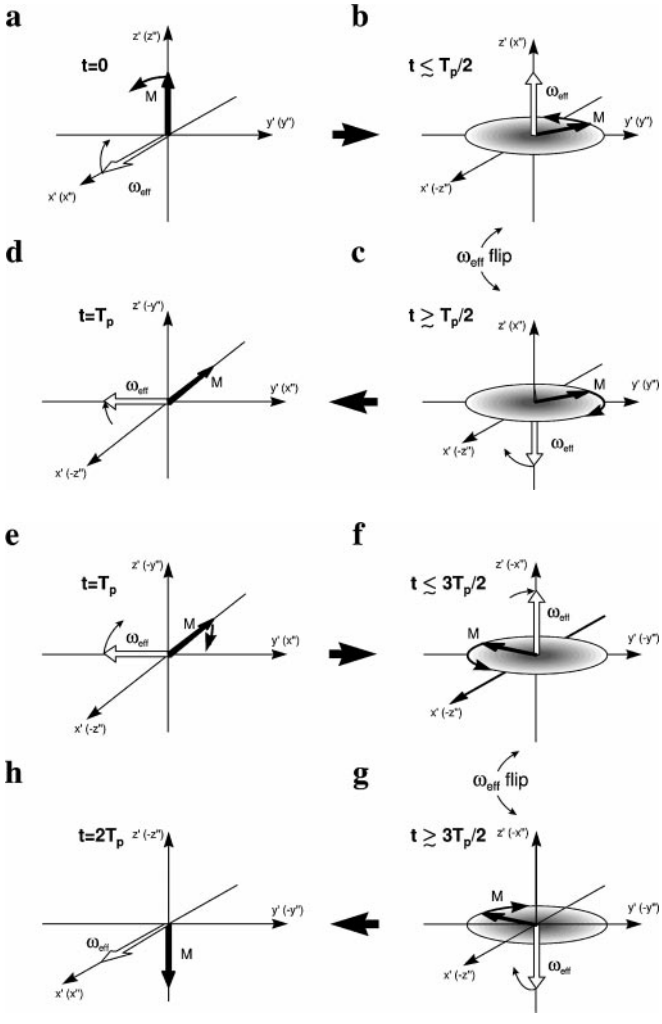

FIG. 11. (a–d) Evolution of $\boldsymbol{\omega}_{\mathbf{eff}}$ and $\mathbf{M}$ in the ω_{RF} frame during a 90° BIR-1 (and the first half of a 180° BIR-4). Thick, curved arrows represent precession of $\mathbf{M}$ around $\boldsymbol{\omega}_{\mathbf{eff}}$. The evolution of $\boldsymbol{\omega}_{\mathbf{eff}}$ is implied by the thin, curved arrows and the orientation of the ω_{eff} frame at each time point ($t = 0$, $T_{\mathrm{p}}/2$, and T_{p}) is indicated by the double primed axes in parentheses. $\boldsymbol{\omega}_{\mathbf{eff}}$ evolves toward z' (a), while $\mathbf{M}$ remains perpendicular to it and disperses due to B_1 inhomogeneity (b). At $t = T_{\mathrm{p}}/2$, $\boldsymbol{\omega}_{\mathbf{eff}}$ is instantaneously inverted and the transverse component of $\boldsymbol{\omega}_{\mathbf{eff}}$ is shifted by 270° (c). During the second half of BIR-1, $\boldsymbol{\omega}_{\mathbf{eff}}$ evolves toward $-y'$, and drives $\mathbf{M}$ back to its initial coherence, which now takes place along $-x'$ of the ω_{RF} frame (d). This represents the final state produced by a 90° BIR-1 and the halfway condition for a 180° BIR-4. (e–h) Second half of a 180° BIR-4. $\boldsymbol{\omega}_{\mathbf{eff}}$ continues to evolve from the previous state (d) toward z' (e). The process of dispersion (f) and coherence recovery (g) repeats with the second $\boldsymbol{\omega}_{\mathbf{eff}}$ flip accompanied by a $-270°$ phase shift. The final state (h) is achieved with $\boldsymbol{\omega}_{\mathbf{eff}}$ along its initial orientation, but with $\mathbf{M}$ inverted in the ω_{RF} frame.

second integrals in Eq. [34] may be unequal, in which case the net rotation of $\mathbf{M}$ about $\boldsymbol{\omega}_{\mathbf{eff}}$ is no longer zero (i.e., a rotary echo is no longer formed in the ω_{eff} frame). As described further below, this problem is eliminated with BIR-4, which is essentially double BIR-1. However, a second unavoidable problem arises because the initial orientation of $\boldsymbol{\omega}_{\mathbf{eff}}$ tilts out of the transverse plane by the angle

$$\alpha(0) = \arctan\left(\frac{\Omega}{\omega_1^{\max}}\right), \qquad [35]$$

where $\omega_1^{\max} = \omega_1(0)$. As $|\Omega|$ increases, $\boldsymbol{\omega}_{\mathbf{eff}}(0)$ acquires an increasing component along z', and as a result, an increasing component of the initial longitudinal magnetization is spin locked with $\boldsymbol{\omega}_{\mathbf{eff}}$. In BIR-4, the component of $\mathbf{M}$ that becomes spin-locked with $\boldsymbol{\omega}_{\mathbf{eff}}$ is returned to z' at the conclusion of the pulse, since the initial ($t = 0$) and final ($t = T_{\mathrm{p}}$) orientations of $\boldsymbol{\omega}_{\mathbf{eff}}$ are the same. Thus, the desired flip angle is not achieved for an increasing fraction of $\mathbf{M}$ as $|\Omega|$ increases. Like conventional RF pulses, the only way to minimize this problem, and thus broaden the bandwidth, is to increase the RF amplitude ($\omega_1^{\max}$) used in BIR pulses. Thus, BIR pulses cannot produce increasingly wide bandwidths with arbitrarily low peak RF power as can be achieved with the classical adiabatic passages discussed above.

The complete sequence of diagrams in Fig. 11 depicts the vector motions of BIR-4, which is a composite adiabatic pulse consisting of four adiabatic segments. The third segment begins (Fig. 11e) where BIR-1 ends (Fig. 11d). A phase shift ($\Delta\phi$) of the middle two segments of BIR-4 creates a flip angle equal to θ when

$$\Delta\phi = \frac{\theta}{2} + 180°. \qquad [36]$$

The rotation axis for θ is determined by the initial phase of $\boldsymbol{\omega}_{\mathbf{1}}$ in BIR-4 (x' in the present example). As shown further below, ψ_{tot} is always zero with BIR-4, provided that ω_0 is included in the sweep range, $\omega_{\mathrm{RF}}(t)$.

IVC. Derivation of BIR Pulses by Recursive Expansion

Composite pulses have been derived by a variety of approaches. One class of methods which has proven to be particularly successful is based on the general principles of similarity transformations (*44*, *76*, *77*). By these methods, pulses that are related by a similarity transformation are combined to produce a longer pulse that provides a higher degree of compensation for some experimental non-ideality, such as resonance offset. Still greater compensation can be achieved by repeating this process on the compensated pulse. This expansion procedure can be repeated as many times as necessary to attain the desired degree of compensation. This general approach has been used to derive some of the best composite pulses available today, including broadband super cycles used in spin decoupling (e.g., MLEV (*77*) and WALTZ (*78*)).

A related approach used to derive composite pulses is based on a recursive expansion (*38*). This procedure is most easily conducted in the PM frame (that rotates with the carrier ω_{c}) using a phase-modulated form of the pulse (instead of the FM

function). To construct a composite *adiabatic* pulse by recursive expansion, a starting element must be chosen which should be a pulse that transforms I_z into any combination of I_x and I_y. In the derivation of BIR pulses, this starting element can be any AHP. A propagation operator P_0 is used to describe the action of this AHP. The second step in the recursive expansion procedure is to form the inverse sequence $(P_0)^{-1}$ by time reversal and phase inversion, or alternatively by omitting the element P_0 from some very cyclic pulse sequence. Although the former method (time reversal and phase inversion) is an exact inverse sequence for the center isochromat only ($\Omega = 0$), BIR pulses derived by this simple approach have the shortest possible lengths. In the final step of the process, the inverse propagator is phase-shifted by the desired flip angle θ and then concatenated to give the sequence $(P_\theta)^{-1}(P_0)$, which is the simplest of the adiabatic plane rotation pulses, BIR-1.

A related approach, the symmetric recursive expansion procedure by Garwood and Ke (*47*), yields symmetric sequences with greater tolerance to resonance offsets ($\Omega \neq 0$), although at the expense of doubling the length. To produce a symmetric sequence by this procedure, the inverse sequence $(P_0)^{-1}$ is phase shifted by only $\theta/2$ and then concatenated to give $(P_{\theta/2})^{-1}(P_0)$. Next, this sequence is time reversed to give $(P_\pi)^{-1}(P_{\pi+\theta/2})$, which is then concatenated with the original sequence. The result is a general formula for time-symmetric sequences of arbitrary flip angle θ,

$$(P_\pi)^{-1}\left(P_{\pi+\theta/2}\right)\left(P_{\theta/2}\right)^{-1}(P_0). \qquad [37]$$

Sequence [37] yields BIR-4 when P_0 is an AHP. Regardless of whether chronological order is followed from right to left or vice versa, sequence [37] generates the same spin response since it has reflection symmetry in time.

IVD. Analytical Description of Adiabatic Plane Rotations

Before proceeding with further theoretical analyses of composite adiabatic pulses, we first briefly consider some mathematical tools needed to treat the problem.

When ignoring relaxation, the density operator ρ of the spin system evolves according to the Liouville-von Neumann equation,

$$\dot{\rho}(t) = i[\rho(t), \mathcal{H}(t)], \qquad [38]$$

where $\mathcal{H}(t)$ is the time-dependent Hamiltonian governing the response of the system. In the rotating frame, the Hamiltonian for an isolated spin I can be expressed as

$$\mathcal{H}(t) = \Omega I_z + \mathcal{H}_{\mathrm{RF}}(t). \qquad [39]$$

With a single square pulse, which has constant amplitude, frequency, and phase, the Hamiltonian is simply

$$\mathcal{H}_{\mathrm{RF}} = \omega_1 \exp(-i I_z \phi) I_x \exp(i I_z \phi). \qquad [40]$$

For a time-dependent adiabatic pulse, the equation of motion (Eq. [38]) must be solved according to

$$\rho(t) = U(t)\rho(0)U(t)^{-1}. \qquad [41]$$

The time-dependent propagator $U(t)$ operates on the density operator from the left and is given by

$$U(t) = \overleftarrow{T} \exp\left\{ -i \int_0^t \mathcal{H}(t')\, dt' \right\}, \qquad [42]$$

where $\overleftarrow{T}$ is the Dyson time-ordering operator which places terms in the integration in order of increasing time to the left. The initial density operator is assumed to be in thermal equilibrium, and in the present analysis, is expressed in reduced form

$$I_z = \rho(0). \qquad [43]$$

The action of an adiabatic pulse can be determined by a stepwise evaluation of the elementary rotations produced by a sequence of N square pulses with incremental changes in amplitude and phase. Alternatively, it can be seen from the vector analysis in Fig. 3 that the net effect of an AHP or AFP can be described simply by a set of pure rotations when the adiabatic condition is fulfilled and the perturbation arising from $d\alpha/dt$ in the ω_{eff} frame can be neglected. Accordingly, in the ω_{RF} frame the adiabatic rapid passage is described by the propagator

$$U = \exp(i\phi I_z)\exp(i\Delta\alpha I_y)\exp(-i\phi I_z)\exp(i\psi I_z), \qquad [44]$$

where ϕ is the phase of $\boldsymbol{\omega_1}$, ψ is the total angle of evolution about $\boldsymbol{\omega_{\mathrm{eff}}}$ given by Eq. [33], and $\Delta\alpha$ is the change in the orientation of $\boldsymbol{\omega_{\mathrm{eff}}}$ (i.e., the net sweep angle) given by

$$\Delta\alpha = \alpha(T_{\mathrm{p}}) - \alpha(0). \qquad [45]$$

Equation [44] is valid for any set of $\omega_1(t)$ and $\Delta\omega(t)$ functions, provided that the adiabatic condition (Eq. [11]) is satisfied and that $\boldsymbol{\omega_{\mathrm{eff}}}$ is approximately collinear with the longitudinal axis at $t = 0$. Upon satisfying these requirements, the transformations produced by an adiabatic passage can be described analytically as

$$\begin{aligned} UI_xU^{-1} = {} & I_x(\cos(\psi-\phi)\cos\Delta\alpha\cos\phi - \sin(\psi-\phi)\sin\phi) \\ & + I_y(\sin(\psi-\phi)\cos\phi + \cos(\psi-\phi)\cos\Delta\alpha\sin\phi) \\ & + I_z(\cos(\psi-\phi)\sin\Delta\alpha) \end{aligned} \qquad [46]$$

$$UI_yU^{-1} = I_x(-\sin(\psi-\phi)\cos\Delta\alpha\cos\phi - \cos(\psi-\phi)\sin\phi) + I_y(\cos(\psi-\phi)\cos\phi - \sin(\psi-\phi)\cos\Delta\alpha\sin\phi) + I_z(\sin(\psi-\phi)\sin\Delta\alpha) \quad [47]$$

$$UI_zU^{-1} = I_x(\cos\phi\sin\Delta\alpha) + I_y(\sin\phi\sin\Delta\alpha) + I_z(\cos\Delta\alpha) \quad [48]$$

Similarly, the reverse AHP (Fig. 10b) used for the first segment of BIR-4 has the propagator

$$U = \exp(-i\psi I_z)\exp(i\phi I_z)\exp(i\Delta\alpha I_y)\exp(-i\phi I_z), \quad [49]$$

Equation [49] is valid for any reverse AHP, provided that the adiabatic condition is satisfied and that the final orientation of $\boldsymbol{\omega_{eff}}$ is approximately collinear with the longitudinal axis.

From this point forward, AHP_f and AHP_r are used to denote forward and reverse AHPs, respectively. Accordingly, the four consecutive segments of BIR-4 can be written as $[AHP_r][AHP_f][AHP_r][AHP_f]$. This sequence describes the order by which Eqs. [44] and [49] are multiplied to yield the BIR-4 propagator,

$$U = \exp(i\phi I_z)\exp(i\Delta\alpha_f I_y)\exp(i\psi_f I_z)\exp(i\Delta\phi I_z) \times \exp(i(\Delta\alpha_r+\Delta\alpha_f)I_y)\exp(-i\Delta\phi I_z)\exp(i(\psi_r+\psi_f)I_z) \times \exp(-i\psi_r I_z)\exp(i\Delta\alpha_r I_y)\exp(-i\phi I_z), \quad [50]$$

where subscripts f and r denote angles associated with AHP_f and AHP_r, respectively, and $\Delta\phi$ is the phase shift of the middle two segments. Transformations induced by BIR-4 can also be described by the rotation matrix

$$\Re = \begin{bmatrix} 1-2\cos^2(\Delta\alpha_f)\sin^2(\Delta\phi) & \cos(\Delta\alpha_f)\sin(2\Delta\phi) & -\sin(2\Delta\alpha_f)\sin^2(\Delta\phi) \\ -\cos(\Delta\alpha_f)\sin(2\Delta\phi) & \cos(2\Delta\phi) & -\sin(\Delta\alpha_f)\sin(2\Delta\phi) \\ -\sin(2\Delta\alpha_f)\sin^2(\Delta\phi) & \sin(\Delta\alpha_f)\sin(2\Delta\phi) & 1-2\sin^2(\Delta\alpha_f)\sin^2(\Delta\phi) \end{bmatrix} \quad [51]$$

To arrive at Eq. [51], it was assumed that $\phi = 0$ (i.e., initially $\boldsymbol{\omega_1}$ is along x') and that $\Delta\alpha_f + \Delta\alpha_r = \pi$ (i.e., $\boldsymbol{\omega_{eff}}$ closely approaches the longitudinal axis at the extremes of the frequency sweep). Note that the ψ dependence has dropped out of Eq. [51], because BIR-4 generates a perfect double rotary echo in the ω_{eff} frame (even when $\psi_r \neq \psi_f$). Dependency on Ω is retained in $\Delta\alpha_f$ (the angle subtended by $\boldsymbol{\omega_{eff}}$ during the AHP segments). For the central isochromat ($\Omega = 0$), $\Delta\alpha_f = 90^\circ$ and Eq. [51] reduces to a pure rotation of angle $2\Delta\phi$ about the x' axis.

Equation [51] describes BIR-4 under ideal conditions (i.e., when the adiabatic condition is perfectly satisfied) and can be used to reveal the best performance that BIR-4 can theoretically attain. In other words, the theoretical performance predicted by Eq. [51] represents a gold standard to gauge the choice of parameters and modulation functions used in BIR-4. In Figs. 12–14, data obtained from Bloch equation simulations using different values of A, T_p, and flip angle θ ($=2\Delta\phi$) are compared with the theoretical predictions given by Eq. [51]. Figures 12 and 13 show the results for $\theta = 90^\circ$ and 45°, respectively. The utility of BIR-4 to perform refocusing in spin-echo experiments is shown in Fig. 14. The magnitude and phase of the refocused magnetization in Fig. 14 were calculated using formula in Ref. (*49*). In all cases, the agreement between Eq. [51] and the Bloch equation improves as the choice of parameters (A and T_p) increases the adiabaticity of the pulses used in the simulations.

IVE. 180° Adiabatic Pulses for Achieving Frequency-Selective Refocusing

BIR pulses were the first adiabatic pulses to accomplish arbitrary flip angles with immunity to B_1 inhomogeneity. Before the introduction of BIR pulses, applications of adiabatic pulses in NMR were generally limited to the two types of adiabatic rotations (90° excitation and population inversion) that tolerated spatial variation of the RF field amplitude, ω_1^{max}. As discussed earlier, certain AFP pulses (e.g., HS1) have abrupt borders ($\pm A$) that sharply demarcate the edges of the inversion bandwidth, and therefore, these pulses are often used in applications requiring frequency-selective inversion. Unfortunately, the excitation bandwidth produced by a truncated AFP (i.e., an AHP) is not sharply demarcated. Because BIR pulses are composed of multiple AHP segments, frequency-selective excitation cannot be performed with current BIR pulses. However, by using similar principles to those used above to construct BIR pulses, multiple AFPs can be combined to create frequency-selective 180° plane rotation pulses. These latter pulses are relevant to the wide variety of spin-echo experiments that utilize frequency-selective refocusing.

The first adiabatic pulse to perform frequency-selective refocusing was developed by Conolly *et al.* (*51*). This refocusing pulse is a composite of a 360° adiabatic sweep and an AFP, separated by a flip of $\boldsymbol{\omega_{eff}}$. The 360° segment serves the sole purpose of creating a rotary echo in ω_{eff} frame that cancels the phase dispersion (ψ) created by the AFP. To accomplish this task, the 360° pulse must have the same duration, ω_1^{max} and A values as the AFP, and should be based on the same AM and FM shapes. As an alternative, a symmetric refocusing pulse has been created from 3 consecutive identical AFPs that have relative lengths $T_p/4$, $T_p/2$, $T_p/4$ (*55*). In the latter composite refocusing pulse, the $\omega_1(t)$ and $\phi(t)$ functions have reflection symmetry in time. Symmetric refocusing pulses of this type offer the advantage of producing a perfectly symmetric response in frequency space (*32*).

Despite the common need for frequency-selective refocusing in many types of experiments, the two adiabatic refocusing pulses described above have yet to gain wide use in NMR. Their major disadvantages include the long duration and high RF power required to perform the three consecutive AFPs that comprise these pulses. However, in an important development, Conolly *et al.* recognized that the phase variation (ψ) generated

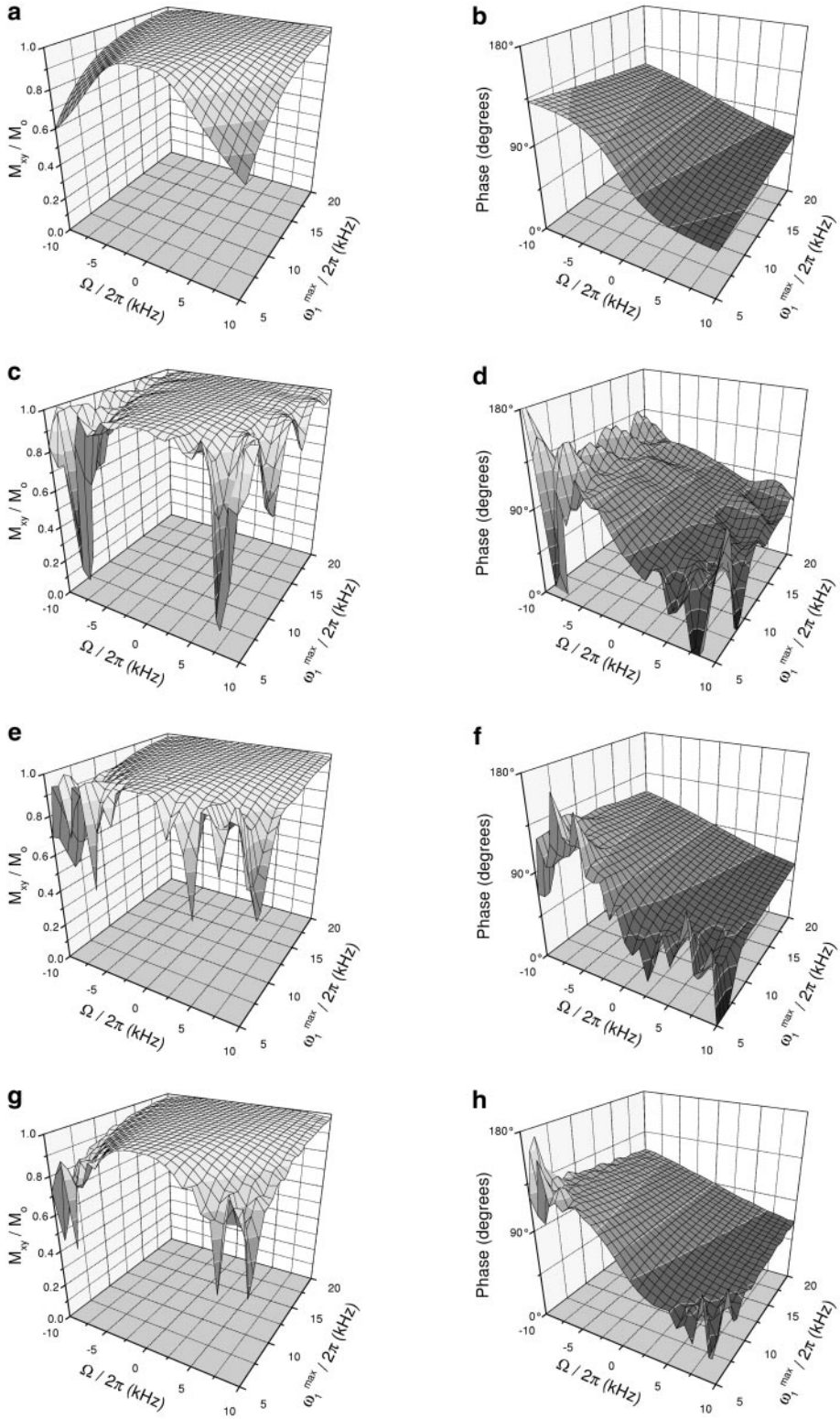

FIG. 12. Bloch equation simulations (c–h) using different values for A and T_p in 90° BIR-4, as compared with (a and b) theoretical predictions assuming 100% adiabatic conditions (Eq. [51]). The left column of plots (a, c, e, g) shows normalized transverse magnetization M_{xy}/M_0 as a function of frequency offset Ω and peak RF intensity ω_1^{max}, while the right column (b, d, f, h) presents the phase of that transverse magnetization as a function of the same parameters. (c–h) Simulations of 90° BIR-4 based on the tanh/tan modulation functions for (c and d) $A/2\pi = 25$ kHz and $T_p = 1$ ms; (e and f) $A/2\pi = 100$ kHz and $T_p = 1$ ms; (g and h) $A/2\pi = 50$ kHz and $T_p = 2$ ms.

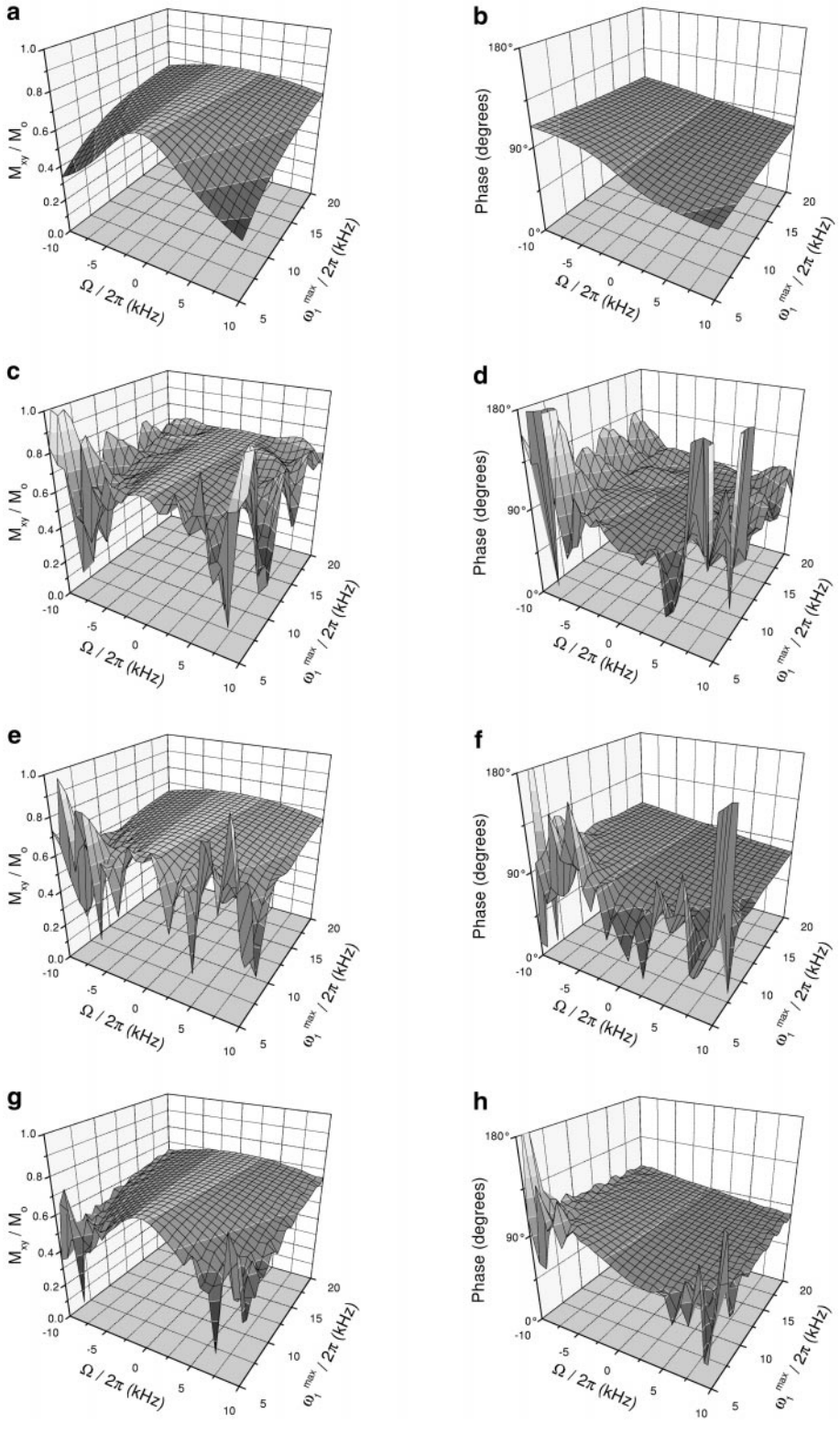

FIG. 13. Bloch equation simulations (c–h) using different values for A and T_p in 45° BIR-4, as compared with (a and b) theoretical predictions assuming 100% adiabatic conditions (Eq. [51]). The left column of plots (a, c, e, g) shows normalized transverse magnetization M_{xy}/M_0 as a function of frequency offset $\mathbf{\Omega}$ and peak RF intensity $\omega_1^{\max}$, while the right column (b, d, f, h) presents the phase of that transverse magnetization as a function of the same parameters. (c–h) Simulations of 45° BIR-4 based on the tanh/tan modulation functions for (c and d) $A/2\pi = 25$ kHz and $T_p = 1$ ms; (e and f) $A/2\pi = 100$ kHz and $T_p = 1$ ms; (g and h) $A/2\pi = 50$ kHz and $T_p = 2$ ms.

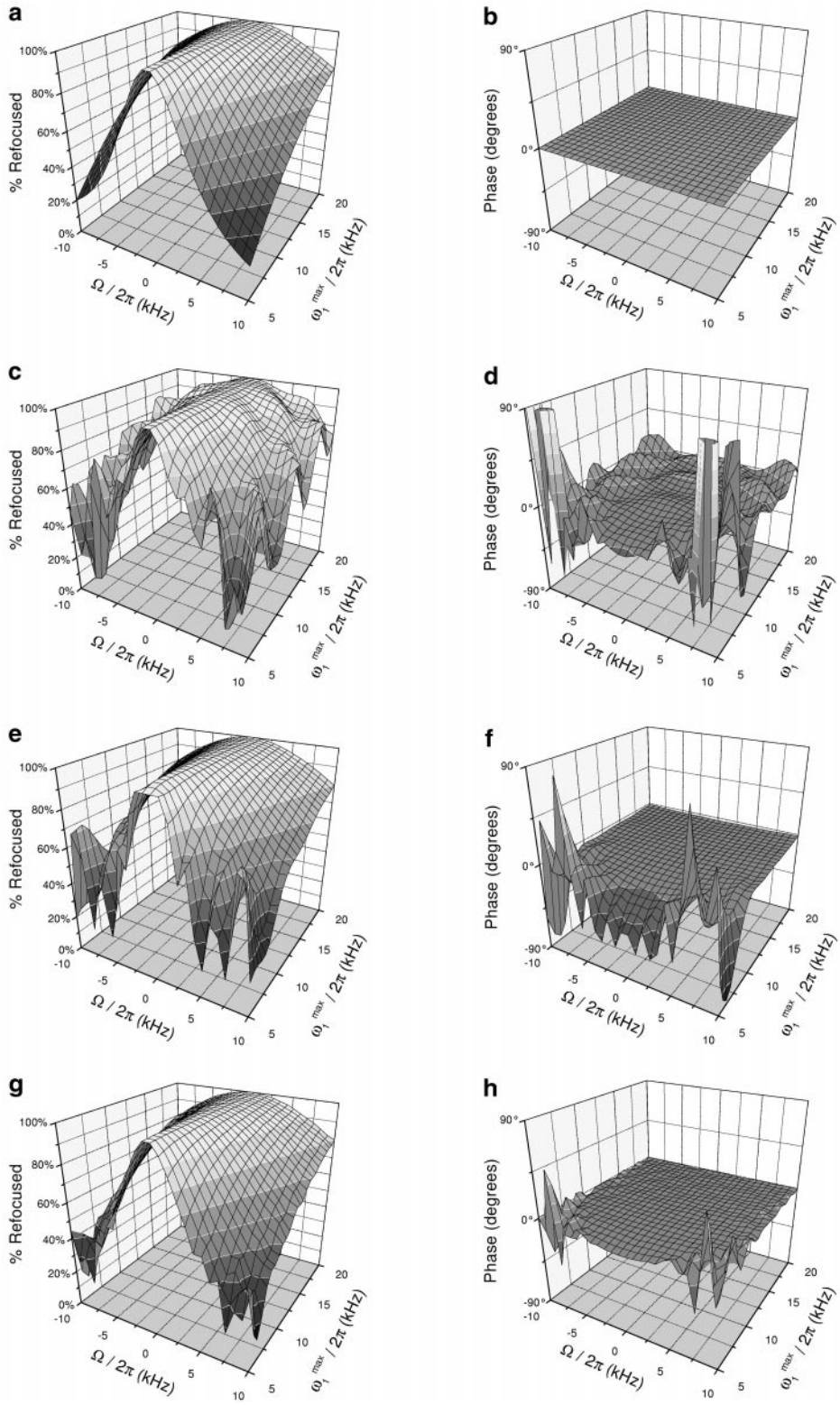

FIG. 14. Bloch equation simulations (c–h) using different values for A and T_p in 180° BIR-4, as compared with (a and b) theoretical predictions assuming 100% adiabatic conditions (Eq. [51]). The left column of plots (a, c, e, g) shows the percentage of the magnetization refocused by a 180° BIR-4 plane rotation pulse as a function of frequency offset Ω and peak RF intensity ω_1^{max}, while the right column (b, d, f, h) presents the phase as a function of the same parameters. (c–h) Simulations of 180° BIR-4 based on the tanh/tan modulation functions for (c and d) $A/2\pi = 25$ kHz and $T_p = 1$ ms; (e and f) $A/2\pi = 100$ kHz and $T_p = 1$ ms; (g and h) $A/2\pi = 50$ kHz and $T_p = 2$ ms.

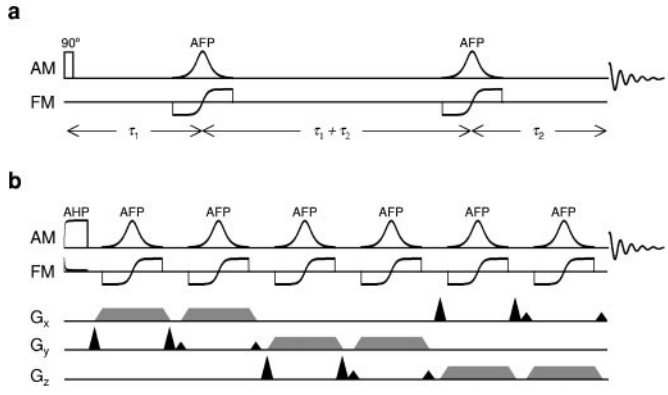

FIG. 15. (a) Double spin-echo sequence using two AFPs. (b) LASER sequence designed for localized spectroscopy. Refocusing is performed by three pairs of broadband AFPs applied in the presence of B_0 gradients (G_x, G_y, G_z). In the present implementation, each AFP pulse is a hyperbolic secant (HS1) pulse (*57*).

by a single AFP could be compensated using two AFPs in a double spin-echo sequence (*68*). Versions of this sequence (Fig. 15a) are gaining wide use in many areas of NMR. Over the past decade, *in vivo* NMR sequences have often exploited the features of double spin echoes to overcome problems arising from B_1 inhomogeneity in imaging and localized spectroscopy (e.g., (*79, 80*)). More recently, Hwang and Shaka extended the principles of double spin echoes and referred to the technique as "excitation sculpting" (*81*). By analyzing spin echoes with propagation operators, they rigorously showed that the phase variation (ψ) created by any RF pulse (AFP or otherwise) is perfectly compensated in the even echoes (as generated with an even number of pulses). In recent years, excitation sculpting has become commonplace in high resolution NMR sequences, due to its robust performance and the high selectivity of its refocusing profile.

Here we provide an experimental demonstration of the versatility of adiabatic spin-echo sequences in imaging and localized spectroscopy. The spectroscopic sequence, as shown in Fig. 15b, is an adiabatic Carr-Purcell train constructed from three sets of double spin echoes. This sequence was designed for *in vivo* spectroscopy and is called LASER which stands for *l*ocalization by *a*diabatic *se*lective *r*efocusing. With LASER, volume selection is accomplished by three pairs of AFPs, each of which delineates a slice orthogonal to the other two slices in space. The selected volume is at the intersection of the three slices, where the spins are refocused following each AFP pair. Magnetization outside the volume-of-interest is dephased by supplemental crushing gradients as done in excitation sculpting. By selecting slices with pairs of HS1 pulses that produce excellent refocusing profiles, the edges of volume are extremely sharp and the signal-to-noise ratio from inside the volume is maximized. Because the spins repetitively receive 180° flips, the sequence also offers the advantages of a Carr-Purcell train. Specifically, anti-phase coherence resulting from J coupling and apparent T_2 shortening arising from diffusion and chemical exchange can be reduced (*82–84*). In the standard implementation, an AHP is typically used for excitation, although any choice of excitation pulse (or sequence) can be used. Figure 16 shows a representative image

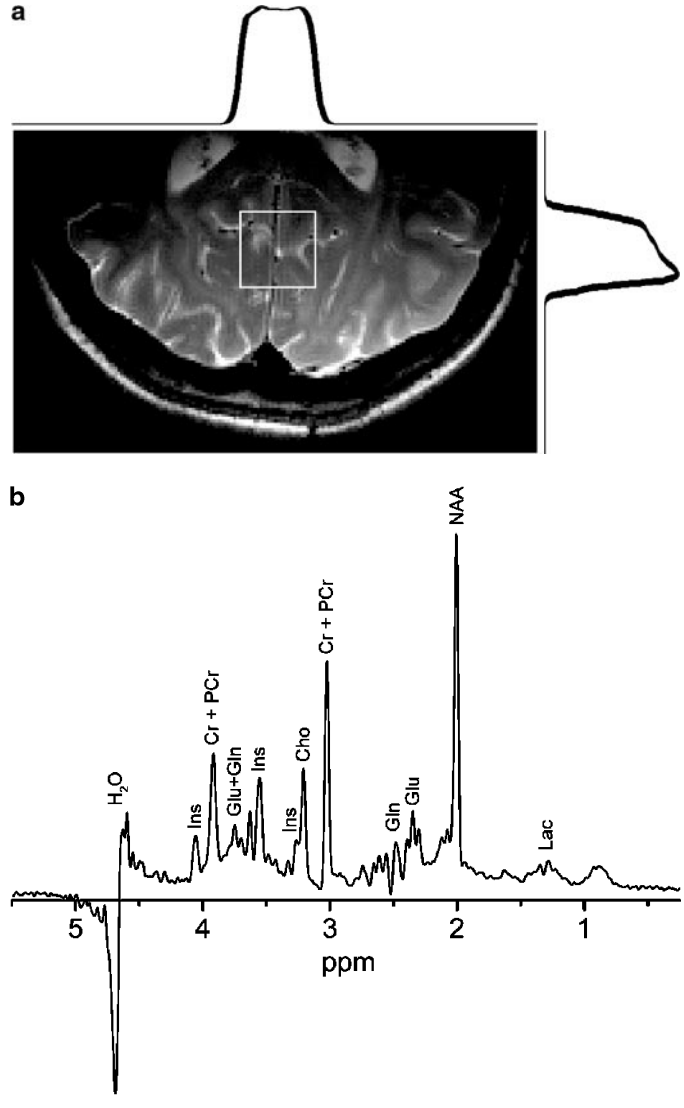

FIG. 16. Human brain imaging and spectroscopy using adiabatic spin-echo sequences. Data were acquired at 4 Tesla using a circularly polarized surface coil for RF transmission and signal reception. (a) Image acquired with a double spin-echo sequence using repetition time = 2.5 s and echo time = 80 ms. The white box shows the position of the localized volume acquired with the sequence in Fig. 15b. To demonstrate the effectiveness of the volume selection, projections of the voxel were acquired with a gradient recalled echo sequence appended to the LASER sequence. (b) Water-suppressed ^{1}H spectrum acquired from the indicated $(2\ \text{cm})^3$ volume of brain. This spectrum was acquired in 64 excitations using repetition time = 6 s and echo time = 36 ms. The AFPs were HS1 pulses with $BW = 5.5$ kHz and $T_p = 3.6$ ms. The supplemental spoiler gradients (black triangles in Fig. 15b) had amplitudes of 3.2 and 1.1 G/cm. Water suppression was performed with the VAPOR technique (*87*). Mild resolution enhancement was used in processing. Abbreviations used for peak assignments are: inositol (Ins), creatine (Cr), phosphocreatine (PCr), glutamate (Glu), glutamine (Gln), choline compounds (Cho), N-acetyl aspartate (NAA), and lactate (Lac).

and water-suppressed ^{1}H spectrum of human brain acquired with adiabatic spin-echo sequences. These results were obtained at 4 Tesla with a 14 cm surface coil placed on the posterior side of the head. The high quality of volume selection with LASER can be seen from the projection profiles of the selected volume plotted along the edges of the double spin-echo image (Fig. 16a). The ^{1}H spectrum (Fig. 16b) acquired with LASER displays excellent spectral resolution and signal-to-noise despite having been acquired from only 8 ml of tissue in just 6.4 minutes.

V. CONCLUSIONS

In this work, adiabatic pulses were analyzed using a classical description suitable for isolated spins. In the presence of more complex spin interactions such as scalar or dipolar coupling, it may be necessary to invoke quantum mechanics to obtain accurate descriptions of the effects of adiabatic pulses on the spin systems (*85, 86*). Likewise, our optimizations of modulation functions were guided by the adiabatic condition, but other approaches such as recursive expansion (*38, 47*) and computer optimizations (*46*) may yield further improvements.

In some types of high field NMR experiments, achieving broad bandwidths with conventional RF pulses is problematic because the bandwidth of such pulses is proportional to and limited by the available $\omega_1^{\max}$. As shown above, pulses that are based on the principles of adiabatic rapid-passage offer a unique way to circumvent this problem, since their bandwidth is limited by the RF energy contained in the pulse, not the RF amplitude. Adiabatic pulses also offer a way to minimize sensitivity losses and to avoid the creation of unwanted coherences in multi-pulse NMR experiments transmitted with an inhomogeneous B_1. Finally, by being highly immune to changes in certain experimental conditions (e.g., the setting of $\omega_1^{\max}$), adiabatic pulses offer a means to begin automating many complex NMR experiments.

In recent years, the number of topics related to the development and application of adiabatic pulses has rapidly expanded. Here we have attempted to show just some of the ways that adiabatic pulses can be tailored to perform efficiently and how they can be designed to satisfy specific experimental needs. This work is by no means a comprehensive review of adiabatic pulses, since it describes only some of the most common forms of adiabatic pulses and a limited set of design methods. Upon considering the breadth of progress in this area, together with the inevitable developments yet to come, there is every reason to believe that adiabatic pulses will become even more ubiquitous in the future.

ACKNOWLEDGEMENTS

The authors gratefully acknowledge many contributions to this work by our colleagues Drs. A. Tannus, R. A. de Graaf, T.-L. Hwang, Y. Ke, A. J. Johnson, P. C. M. van Zijl, R. Gruetter, and K. Ugurbil. We also thank Mr. David Busch for valuable discussions and for producing some of the illustrations. This work was supported by NIH Grants RR08079, CA64338 and CA79732.

REFERENCES

1. R. R. Ernst and W. A. Anderson, Application of Fourier transformation spectroscopy to magnetic resonance, *Rev. Sci. Instrum.* **37,** 93–101 (1966).
2. E. M. Purcell, H. C. Torrey, and R. V. Pound, Resonance absorption by nuclear magnetic moments in a solid, *Phys. Rev.* **69,** 37 (1946).
3. F. Bloch, W. W. Hansen, and M. Packard, Nuclear induction, *Phys. Rev.* **69,** 127 (1946).
4. A. Abragam, The principles of nuclear magnetism. 1978: Clarendon Press.
5. J. Baum, R. Tycko, and A. Pines, Broadband and adiabatic inversion of a two-level system by phase-modulated pulses, *Phys. Rev. A* **32,** 3435–3447 (1985).
6. S. Conolly, D. Nishimura, and A. Macowski, Variable-rate selective excitation, *J. Magn. Reson.* **78,** 440–458 (1988).
7. K. Ugurbil, M. Garwood, and A. Rath, Optimization of modulation functions to improve insensitivity of adiabatic pulses to variations in B_1 magnitude, *J. Magn. Reson.* **80,** 448–469 (1988).
8. C. J. Hardy, W. A. Edelstein, and D. Vatis, Efficient adiabatic fast passage for NMR population inversion in the presence of radiofrequency field inhomogeneity and frequency offsets, *J. Magn. Reson.* **66,** 470–482 (1986).
9. T. E. Skinner and P.-M. L. Robitaille, General solutions for tailored modulation profiles in adiabatic excitation, *J. Magn. Reson.* **98,** 14–23 (1992).
10. T. E. Skinner and P. M. L. Robitaille, Adiabatic excitation using $\sin^2$ amplitude and $\cos^2$ frequency modulation functions, *J. Magn. Reson. A* **103,** 34 (1993).
11. E. Kupce and R. Freeman, Stretched adiabatic pulses for broadband spin inversion, *J. Magn. Reson. A* **117,** 246 (1995).
12. E. Kupce and R. Freeman, Optimized adiabatic pulses for wideband spin inversion, *J. Magn. Reson. A* **118,** 229–303 (1996).
13. A. Tannús and M. Garwood, Improved performance of frequency-swept pulses using offset-independent adiabaticity, *J. Magn. Reson. A* **120,** 133–137 (1996).
14. R. J. Ordidge, M. Wylezinska, J. W. Hugg, E. Butterworth, and F. Franconi, Frequency offset corrected inversion (FOCI) pulses for use in localized spectroscopy, *Magn. Reson. Med.* **36,** 562–566 (1996).
15. J. Shen, Use of amplitude and frequency transformations to generate adiabatic pulses of wide bandwidth and low RF power deposition, *J. Magn. Reson. B* **112,** 131–140 (1996).
16. D. Rosenfeld, S. L. Panfil, and Y. Zur, Design of selective adiabatic inversion pulses using the adiabatic condition, *J. Magn. Reson.* **129,** 115–124 (1997).
17. M. Garwood, B. Nease, Y. Ke, R. A. de Graaf, and H. Merkle, Simultaneous compensation for B_1 inhomogeneity and resonance offsets by a multiple-quantum NMR sequence using adiabatic pulses, *J. Magn. Reson. A* **112,** 272–274 (1995).
18. P. C. M. van Zijl, T.-L. Hwang, M. O'Neil Johnson, and M. Garwood, Optimized excitation and automation for high-resolution NMR using B_1-insensitive rotation pulses, *J. Am. Chem. Soc.* **118,** 5510–5511 (1996).
19. T.-L. Hwang, P. C. M. van Zijl, and M. Garwood, Asymmetric adiabatic pulses for NH selection, *J. Magn. Reson.* **138,** 173–177 (1999).
20. W. Peti, C. Griesinger, and W. Bermel, Adiabatic TOCSY for C,C and H,H J-transfer, *J Biomol NMR* **18,** 199–205 (2000).
21. V. J. Basus, P. D. Ellis, H. D. W. Hill, and J. S. Waugh, Utilization of chirp frequency modulation with 180°-phase modulation for heteronuclear spin decoupling, *J. Magn. Reson.* **35,** 19–37 (1979).
22. P. R. Luyten, G. Bruntink, F. M. Sloff, J. W. A. H. Vermeulen, J. I. van der Heijden, J. A. den Hollander, and A. Heerschap, Broadband proton decoupling in human ^{31}P NMR spectroscopy, *NMR Biomed.* **1,** 177–183 (1989).

23. Z. Starcuk, K. Bartusek, and Z. Starcuk, Heteronuclear broadband spin-flip decoupling with adiabatic pulses, *J. Magn. Reson. A* **107,** 24–31 (1994).
24. M. R. Bendall, Broadband and narrowband spin decoupling using adiabatic spin flips, *J. Magn. Reson. A* **112,** 126–129 (1995).
25. E. Kupce and R. Freeman, Adiabatic pulses for wideband inversion and broadband decoupling, *J. Magn. Reson. A* **115,** 273–276 (1995).
26. R. Fu and G. Bodenhausen, Ultra-broadband decoupling, *J. Magn. Reson. A* **117,** 324–325 (1995).
27. J. Pfeuffer, I. Tkac, I.-Y. Choi, H. Merkle, K. Ugurbil, M. Garwood, and R. Gruetter, Localized in vivo ^{1}H NMR detection of neurotransmitter labeling in rat brain during infusion of [1-^{13}C]D-glucose, *Magn. Reson. Med.* **41,** 1077–1083 (1999).
28. H. Barfuss, H. Fischer, D. Hentschel, R. Ladebeck, A. Oppelt, and R. Wittig, *In vivo* magnetic resonance imaging and spectroscopy of humans with a 4T whole-body magnet, *NMR Biomed.* **3,** 31–45 (1990).
29. M. H. Levitt and R. Freeman, NMR population inversion using a composite pulse, *J. Magn. Reson.* **33,** 473–476 (1979).
30. R. Freeman, S. P. Kempsell, and M. H. Levitt, Radiofrequency pulse sequences which compensate their own imperfections, *J. Magn. Reson.* **38,** 453–479 (1980).
31. M. H. Levitt and R. Freeman, Compensation for pulse imperfectons in NMR spin-echo experiments, *J. Magn. Reson.* **43,** 65–80 (1981).
32. M. H. Levitt, Symmetrical composite pulse sequence for NMR population inverion. I. Compensation for radiofrequency field inhomogeneity, *J. Magn. Reson.* **48,** 234–264 (1982).
33. M. H. Levitt, Symmetrical composite pulse sequence for NMR population inverion. II. Compensation for resonance offset, *J. Magn. Reson.* **50,** 95–110 (1982).
34. J. S. Waugh, Theory of broadband spin decoupling, *J. Magn. Reson.* **50,** 30–49 (1982).
35. A. J. Shaka and R. Freeman, Composite pulses with dual compensation, *J. Magn. Reson.* **55,** 487–493 (1983).
36. A. J. Shaka and A. Pines, Symmetric phase-alternating composite pulses, *J. Magn. Reson.* **71,** 495–503 (1983).
37. J. Baum, R. Tycko, and A. Pines, Broadband population inversion by phase modulated pulses, *J. Chem. Phys.* **79,** 4643–4647 (1983).
38. M. H. Levitt and R. R. Ernst, Composite pulses constructed by a recursive expansion procedure, *J. Magn. Reson.* **55,** 247 (1983).
39. M. H. Levitt and R. R. Ernst, Improvement of pulse performance in N.M.R. coherence transfer experiments. A compensated INADEQUATE experiment, *Mol. Phys.* **50,** 1109–1124 (1983).
40. R. Tycko, Broadband population inversion, *Phys. Rev. Lett.* **51**, 775–777 (1983).
41. R. Tycko, A. Pines, and J. Guckenheimer, Fixed point theory of iteractive excitation schemes in NMR, *J. Chem. Phys.* **83,** 2775–2802 (1985).
42. R. Tycko, H. M. Cho, E. Schneider, and A. Pines, Composite pulses without phase distortion, *J. Magn. Reson.* **61,** 90–101 (1985).
43. C. Counsell, M. H. Levitt, and R. R. Ernst, Analytical theory of composite pulses, *J. Magn. Reson.* **63,** 133–141 (1985).
44. M. H. Levitt, Composite pulses, *Prog. Nuc. Magn. Reson. Spectrosc.* **18,** 61–122 (1986).
45. A. J. Shaka and A. Pines, Symmetric phase-alternating composite pulses, *J. Magn. Reson.* **71,** 495–503 (1987).
46. C. S. Poon and R. M. Henkelman, Robust refocusing pulses of limited power, *J. Magn. Reson. A* **116,** 161–180 (1995).
47. M. Garwood and Y. Ke, Symmetric pulses to induce arbitrary flip angles with compensation for RF inhomogeneity and resonance offsets, *J. Magn. Reson.* **94,** 511–525 (1991).
48. K. Ugurbil, M. Garwood, and M. R. Bendall, Amplitude and frequency modulated pulses to achieve 90° plane rotations with inhomogeneous B_1 fields, *J. Magn. Reson.* **72,** 177–185 (1987).
49. R. M. Bendall, K. Ugurbil, M. Garwood, and D. T. Pegg, Adiabatic refocusing pulse which compensates for variable RF power and off-resonance effects, *Magn. Reson. Med.* **4,** 493–499 (1987).
50. K. Ugurbil, M. Garwood, A. R. Rath, and M. R. Bendall, Amplitude- and frequency/phase-modulated refocusing pulses that induce plane rotations even in the presence of inhomogeneous B_1 fields, *J. Magn. Reson.* **78,** 472–497 (1988).
51. S. Conolly, D. Nishimura, and A. Macovski, A selective adiabatic spin-echo pulse, *J. Magn. Reson.* **83,** 324–334 (1989).
52. B. A. Inglis, K. D. Sales, and S. C. R. Williams, BIRIANI, a new composite adiabatic pulse for water-suppressed proton NMR spectroscopy, *J. Magn. Reson. B* **105,** 61–66 (1994).
53. R. A. de Graaf, Y. Luo, M. Terpstra, H. Merkle, and M. Garwood, A new localization method using an adiabatic pulse, BIR-4, *J. Magn. Reson. B* **106,** 245–252 (1995).
54. R. A. de Graaf, K. Nicolay, and M. Garwood, Single-shot, B_1-insensitive slice selection with a gradient-modulated adiabatic pulse, BISS-8, *Magn. Reson. Med.* **35,** 652–657 (1996).
55. T.-L. Hwang, P. C. M. van Zijl, and M. Garwood, Broadband adiabatic refocusing without phase distortion, *J. Magn. Reson.* **124,** 250–254 (1997).
56. J. Shen, Adiabatic slice-selective excitation for surface coils, *J. Magn. Reson.* **124,** 72–79 (1997).
57. M. S. Silver, R. I. Joseph, and D. I. Hoult, Highly selective $\pi/2$ and π pulse generation, *J. Magn. Reson.* **59,** 347–351 (1984).
58. F. T. Hioe, Solution of Bloch equations involving amplitude and frequency modulations, *Phys. Rev. A* **30,** 2100–2103 (1984).
59. S. L. McCall and E. L. Hahn, Self-induced transparency, *Phys. Rev.* **183,** 457–485 (1969).
60. J. J. Dunand and J. Delayre. U.S. patent 3,975,675 (1976).
61. I. Solomon, Rotary spin echoes, *Phys. Rev. Lett.* **2,** 301–305 (1959).
62. D. Kunz, Use of frequency-modulated radiofrequency pulses in MR imaging experiments, *Magn. Reson. Med.* **3,** 377 (1986).
63. M. R. Bendall and D. T. Pegg, Uniform sample excitation with surface coils for *in vivo* spectroscopy by adiabatic rapid half passage, *J. Magn. Reson.* **67,** 376–381 (1986).
64. A. J. Johnson, M. Garwood, and K. Ugurbil, Slice selection with gradient-modulated adiabatic excitation despite the presence of large B_1 inhomogeneities, *J. Magn. Reson.* **81,** 653–660 (1989).
65. Z. Wang, Theory of selective excitation by scaled frequency-amplitude sweep, *J. Magn. Reson.* **81,** 617 (1989).
66. J.-M. Böhlen, M. Rey, and G. Bodenhausen, Refocusing with chirped pulses for broadband excitation without phase dispersion, *J. Magn. Reson.* **84,** 191 (1989).
67. M. Garwood and K. Ugurbil, *B_1 insensitive adiabatic RF pulses, in* "NMR Basic Principles and Progress," J. Seelig and M. Rudin, Editors. 1991, Springer-Verlag, Berlin. p. 109–147.
68. S. Conolly, G. Glover, D. Nishimura, and A. Macovski, A reduced power selective adiabatic spin-echo pulse sequence, *Magn. Reson. Med.* **18,** 28–38 (1991).
69. Y. Ke, D. G. Schupp, and M. Garwood, Adiabatic DANTE sequences for B_1-insensitive narrowband inversion, *J. Magn. Reson.* **23,** 96–108 (1992).
70. J. Slotboom, B. A. P. M. Vogels, J. G. de Haan, J. H. N. Creyghton, G. Quack, R. A. F. M. Chamuleau, and W. M. M. J. Bovëe, Proton resonance spectroscopy study of the effects of L-ornithine-L-aspartate on the development of encephalopathy, using localization pulses with reduced specific absorption rate, *J. Magn. Reson. B* **105,** 147–156 (1994).

71. R. A. de Graaf, Y. Luo, M. Garwood, and K. Nicolay, B_1-insensitive, single-shot localization and water suppression, *J. Magn. Reson. B* **113,** 35–45 (1996).
72. D. Rosenfeld, S. L. Panfil, and Y. Zur, Analytic solutions of the Bloch equation involving asymmetric amplitude and frequency modulations, *Phys. Rev. A* **54,** 2439–2443 (1996).
73. D. Rosenfeld, S. L. Panfil, and Y. Zur, Design of adiabatic pulses for fat-suppression using analytic solutions of the Bloch equation, *Magn. Reson. Med.* **37,** 793–801 (1997).
74. A. Tannús and M. Garwood, Adiabatic pulses, *NMR Biomed.* **10,** 423–434 (1997).
75. W. S. Warren and M. S. Silver, *Adv. Magn. Reson.* **12,** 247–384 (1988).
76. J. S. Waugh, Systematic procedure for constructing broadband decoupling sequences, *J. Magn. Reson.* **49,** 517–521 (1982).
77. M. H. Levitt, R. Freeman, and T. Frenkiel, Broadband decoupling in high resolution nuclear magnetic resonance spectroscopy, *Adv. Magn. Reson.* **11,** 47–110 (1983).
78. A. J. Shaka, J. Keeler, T. Frenkiel, and R. Freeman, An improved sequence for broadband decoupling: WALTZ-16, *J. Magn. Reson.* **52,** 335–338 (1983).
79. D. G. Schupp, H. Merkle, J. M. Ellermann, Y. Ke, and M. Garwood, Localized detection of glioma glycolysis using edited ^{1}H MRS, *Magn. Reson. Med.* **30,** 18–27 (1993).
80. R. A. de Graaf, Y. Luo, M. Terpstra, and M. Garwood, Spectral editing with adiabatic pulses, *J. Magn. Reson. B* **109,** 184–193 (1995).
81. T.-L. Hwang and A. J. Shaka, Water suppression that works. Excitation sculpting using arbitrary waveforms and pulsed field gradients, *J. Magn. Reson. A* **112,** 275–279 (1995).
82. H. Y. Carr and E. M. Purcell, Effects of diffusion on free precession in nuclear magnetic resonance experiments, *Phys. Rev.* **94,** 630–638 (1954).
83. A. Allerhand and E. Thiele, Analysis of Carr-Purcell spin-echo NMR experiments on multiple-spin systems. II. The effect of chemical exchange, *J. Chem. Phys.* **43,** 903–916 (1966).
84. A. Allerhand, Analysis of Carr-Purcell spin-echo NMR experiments on multiple-spin systems. I. The effect of homonuclear coupling, *J. Chem. Phys.* **44,** 1–9 (1966).
85. S. Hediger, B. H. Meier, N. D. Kurur, G. Bodenhausen, and R. R. Ernst, NMR cross polarization by adiabatic passage through the Hartmann-Hahn condition (APHH), *Chem. Phys. Lett.* **223,** 283–288 (1994).
86. S. Capuani, F. D. Luca, L. Marinelli, and B. Maraviglia, Coherence-transfer process by adiabatic pulses, *J. Magn. Reson. Series A* **121,** 1–7 (1996).
87. I. Tkac, Z. Starcuk, I.-Y. Choi, and R. Gruetter, In vivo ^{1}H NMR spectroscopy of rat brain at 1 msec echo time, *Magn. Reson. Med.* **41,** 649–656 (1999).